

Reactionless Motion Control of Free-Floating/Flying Space Manipulators and **its** Applications

Master Thesis Presented to
the Graduate School of Engineering,
Tokyo City University
in Partial Fulfillment of the Requirements
for the Degree of Master of Engineering Course

1481214 Hiroki Sone
Advisor: Prof. Dragomir N. Nenchev
Assoc. Prof. Daisuke Sato

Submission date

Contents

1	Introduction	11
1.1	Space robots	11
1.1.1	Control issues on FFSR	13
1.1.2	Reactionless motion control	14
1.1.3	Energy consumption	16
1.2	Motion/Force control	17
1.3	Aim of this study	17
1.4	Outline of this thesis	18
1.5	The roles of variable's index	19
2	Basic Notation	21
2.1	Modeling of free-floating base robots	21
2.1.1	Kinematics	22
2.1.2	Kinetic energy	23
2.1.3	Inertia submatrices	24
2.1.4	Equation of motion	25
2.2	Momentum conservation law	26
2.2.1	Linear momentum conservation law	26
2.2.2	Angular momentum conservation law	27
2.3	Reaction Null-Space	29
2.3.1	Momentum based derivation	29

2.3.2	Dynamics based derivation	30
2.4	Summary	30
3	Review of Reactionless Motion and Analysis	33
3.1	Reactionless motion control	33
3.2	Qualitative study of reactionless motion	34
3.2.1	Fixed point and bifurcation	36
3.2.2	Details of the fixed point	37
3.3	Summary	38
4	Proposal of Reactionless Tasks	41
4.1	Manipulator model	41
4.1.1	Model description	41
4.1.2	Reactionless motion representation	42
4.2	Inspection task using a hand camera	45
4.2.1	Control command	46
4.2.2	Numerical simulation	47
4.2.3	The algorithmic singularities within the reactionless in- spection task	50
4.3	Point-to-point positioning task	56
4.3.1	The 3-Phase method	57
4.3.2	Verification via numerical simulations	58
4.4	Deployment task	61
4.4.1	Full reactionless task	62
4.5	Summary	64
5	Energy Consumption Analysis	67
5.1	Kinetic energy	67
5.2	Instantaneous minimum energy motion	68
5.3	Motion equivalence	69

<i>CONTENTS</i>	3
5.3.1 Two-DoF planar manipulator	69
5.3.2 Influence arising from parameters variation	70
5.3.3 Four-DoF spatial manipulator	71
5.4 Discussion about the equivalence	72
5.5 Comparison study	74
5.5.1 Simulation condition	74
5.5.2 Simulation results	75
5.6 Summary	76
6 Formulation and Modeling	79
6.1 Formulations	79
6.1.1 OS formulation based control	79
6.1.2 Reaction Null-Space based control	83
6.2 Examples	86
6.2.1 Planar three-DoF manipulator	86
6.2.2 Seven DoF redundant manipulator	91
6.3 Summary	93
7 Analysis on Joint Motion Behavior	97
7.1 Influence of the inertia parameter	97
7.1.1 Analysis through simulations	98
7.1.2 Discussion about the coincidence	99
7.1.3 Verification via numerical simulations	101
7.2 Stabilization of joint motion	103
7.2.1 The velocity-level based acceleration solution	104
7.2.2 Verification via numerical simulations	105
7.3 Summary	106
8 Discussion and Future Research Directions	107
8.1 Conclusions	107

8.2 Future tasks	109
Acknowledgment	111
References	113

List of Figures

1.1	Space robotic systems: (a) Canadarm ©NASA, (b) Canadarm 2 ©NASA, (c) JEMRMS ©JAXA and (d) ETS-VII.	12
2.1	General model of free-floating base robot.	22
2.2	Relationship between a variation of translation and a rotational variation.	28
3.1	A planer two-DoF space manipulator model, whose parameters are $m_i = 100$ kg, $l_i = 1.0$ m ($i = 1, 2$); the base mass is $m_b = 1000$ kg, and its reactionless motion vector field.	35
3.2	The vector field and nullclines for each joint direction with variation r : (a) $r = 0.5$ m, (b) $r = 0.945$ m and (c) $r = 1.5$ m.	37
3.3	This figure shows the determinant of the coupling inertia matrix and the distance between the manipulator CoM and the base one as color map: (a) $\det(\tilde{\mathbf{M}}_{\omega m} \tilde{\mathbf{M}}_{\omega m})$ and (b) the distance between the manipulator CoM and the base one.	38
4.1	Our manipulator model with seven-DoF mechanism at the initial configuration ($\theta_i = 0$ rad, $\forall \theta_i$).	42
4.2	Reactionless motion of the manipulator model: (a) the predominant wrist motion and (b) the elbow folding motion.	44
4.3	Inspection task using the hand camera: (a) target satellite to be refueled of captured and (b) own-satellite attached devices.	45

4.4	Simulation result under the satellite observation mission (Fig. 4.3 (a)).	48
4.5	Simulation result under the inspection of own-satellite mounted devices (Fig. 4.3 (b)).	49
4.6	An example of the algorithmic singularity within the proposed method.	52
4.7	Simulation results under the damped least-squares inverse with numerical filtering.	53
4.8	Simulation results under the singularity consistent method. . .	56
4.9	A motion obtained via the 3-Phase method.	57
4.10	The simulation results under the 3-phase method: (a) the joint velocity and (b) the coupling angular momentum.	59
4.11	The snapshot of the motion obtained via the 3-phase method.	60
4.12	The base attitude deviations under the all methods: (a) 3-phase method, (b) JS-C, (c) IJ-C and (d) TJ-C.	61
4.13	Motion snapshots from the deployment task under reactionless motion control.	63
4.14	The snapshot of the motion under partial reactionless deployment.	64
4.15	The snapshot of the motion under the conventional joint space interpolation.	65
5.1	The distribution of the cost function with the two-DoF model.	70
5.2	This figure shows how the average of C_{ratio} is affected by parameter variation.	71
5.3	The disutribution of cost function with the four-DoF spatial manipulator model: (a) regularly appearing distribution $(\theta_1, \theta_2) = (-3.05, 0.403)$ rad and (b) near the singularity $(\theta_1, \theta_2) = (-\pi, 0)$ rad.	73
5.4	An example of energy consumption comparison.	75
5.5	Comparison of energy consumption under five conditions . . .	76

6.1	Model of n -link manipulator model and its $n + 1$ link control model for the RNS-based controller.	80
6.2	Three-link planar redundant manipulator: (a) real model and (b) control model.	87
6.3	Simulation results of end-effector position and force. The position error is along x -direction, while the force error is represented along z direction, in the end-effector frame.	89
6.4	Simulation results of the joint variables.	90
6.5	Simulation model based on the arm of Rollin' Justin.	92
6.6	Motion control direction is along x axis, while force control direction is along z axis, in the end-effector frame $\{E\}$	93
6.7	Simulation results of end-effector position and force measured in the inertial frame.	94
6.8	Simulation results of joint-space behavior.	95
7.1	The time profiles of the joint velocity and the null-space velocity: the upper part represents the joint velocity; the lower part is the null-space velocity, respectively.	98
7.2	A geometrical interpretation of the RNS constraint: (a) with a small mass of the constrained link and (b) with a large value of the mass.	101
7.3	The root means square of the motion error.	102
7.4	Time profile of the Euclidean norm of the null-space velocity: the line in red represents the velocity based acceleration solution; the line in green stands for the velocity with the damper.	105

List of Tables

4.1	Dynamic model parameters	42
4.2	The maximum value of the base deviation.	60

Chapter 1

Introduction

1.1 Space robots

The first use of a robotic system in space is the Shuttle Remote Manipulator System (SRMS), whose nickname is *Canadarm* (Fig. 1.1 (a)), on Space Shuttle Colombia in 1981 [1]. After that, robotic systems have been employed in various space missions. A well-known space robot is the Space Station Remote Manipulator System (SSRMS) developed by the Canadian Space Agency (CSA). The manipulator was named *Canadarm 2* and has performed several missions, successfully; the most recent mission executed by Canadarm 2 is a catching mission of the H-II Transfer Vehicle (Fig. 1.1 (b)). Canadarm 2 consists of 17-meter long, 7 degree-of-freedom (DoF) symmetric mechanism. As a similar robotic system, the Japan Aerospace Exploration Agency (JAXA) developed the Japanese Experiment Module Remote Manipulator System (JEMRMS) and a small fine arm (SFA) attached on the end of JEMRMS; hence, the combined system has been referred to as JEMRMS/SFA (Fig. 1.1 (c)).

In addition to this kind of space robotic system, free-floating space robots (FFSR), which consists of a satellite base and at least one manipulator arm, are expected to perform future space missions. These missions would be

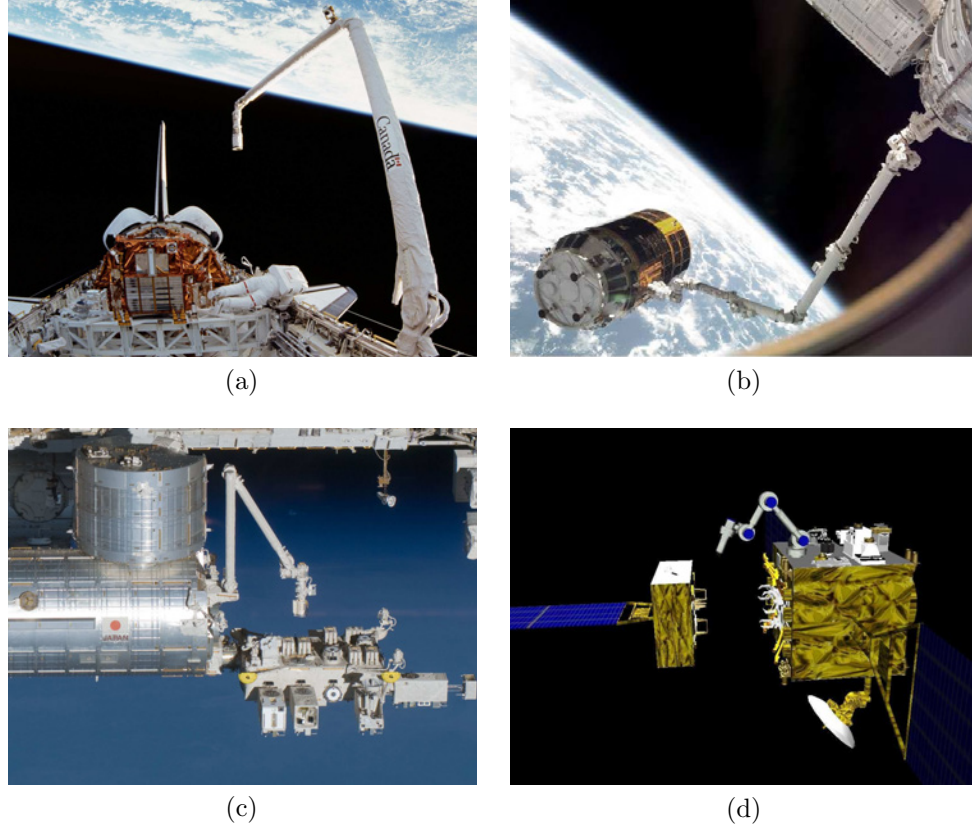


Fig. 1.1: Space robotic systems: (a) Canadarm ©NASA, (b) Canadarm 2 ©NASA, (c) JEMRMS ©JAXA and (d) ETS-VII.

debris removal, construction of large space buildings, servicing for launched satellites and so on. So far, this type of space robots have not been used in practical missions. On the other hand, an experimental robotic system was developed by JAXA around 1997. The robotic system has been referred to as the *Experimental Test Satellite VII* (ETS-VII) [2]. ETS-VII consists of a 2-meter long, 6-DoF manipulator and a 2000 kg class of unmanned satellite (Fig. 1.1 (d)). The system demonstrated some important robotic technologies: autonomous rendezvous and docking (AR&D) and robotic servicing. The robotic servicing includes exchange of orbital replacement unit (ORU),


deployment of a space structure and capturing of a target satellite. As an important results, it was confirmed that the manipulator motions actually induced base motions as indicated from the mechanics theory [3–5]. Hence, specific controller designs for space robots have to be developed in order to execute future space missions, successfully.

1.1.1 Control issues on FFSR

A most significant problem when controlling manipulators in space is the dynamic coupling between the manipulators and the satellite base. The coupling induces a base translation and also rotation. Because of the base motions, control methods that have been employed in terrestrial cannot be applied straightforwardly. To overcome this problem, the information of the base motions has to be taken into account within the control schemes.

An important study considered the above issue was done in [4, 6]. The authors proposed the Generalized Jacobian, which includes a base motion estimated from the linear/angular momentum conservation laws. By using the Jacobian, the correct mapping from task space into the joint space can be obtained. This method can be applied simply by replacing the conventional Jacobian matrix with the generalized one on the terrestrial robot controllers. The resolved motion rate control and the resolved acceleration control with the Generalized Jacobian were verified through numerical simulation. In addition, on the experiment with ETS-VII, the utility of the generalized Jacobian was confirmed under resolved motion rate control [5].

On the other hand, a base rotation itself is a problem because it induces a communication failure between the space robot and the ground control center. To overcome this problem, using gas-jet thruster was considered by some researchers [7]. On the experiment of ETS-VII, under a camera inspection type of mission, the thrusters were used to stabilize the base attitude. However, the fuel for thrusters is finite and its amount determines the life duration

of the space systems. Therefore, attitude devices using electric power such as reaction wheel ~~1~~ has been considered so far [8, 9]. Reaction wheels have been successfully used on zero momentum type of various satellites to stabilize **its** attitude especially against the gravity gradient torque, earth magnetism torque and solar radiation pressure. However, if it is considered that reaction wheels are used to compensate the base reaction induced by a manipulator motion, the output torque  reaction wheels **are quite poor** with respect to the base reaction. To avoid saturation of the reaction wheel signals, the manipulator has to be driven at very low speed. When some repeatable tasks, e.g. observation/inspection or assembly for construction missions are performed, this low speed manipulation is not desirable from the perspective of work efficiency [6]. Hence, developing a control method that generates a manipulator motion inducing a small reaction is **a** important issue **on** space robots.

As a pioneer work ~~of~~ manipulator's reaction control, the disturbance map was developed for free-floating space robots [10]. ~~Using this method, we can visualize the base reaction as a color map on the joint space and can generate a low reaction path through intuitive manner with the color map.~~ However, if the DoF of the system is more than two, it is difficult to apply this method because the color map cannot be displayed in space whose dimension is more than three. In addition, it is difficult to obtain a low reaction motion through the color map, automatically.

1.1.2 Reactionless motion control

A motion generation method was proposed for zero reaction manipulation. This method has been referred to as the *Reaction Null-Space* (RNS) formulation [11–13], and provides a straightforward approach to reactionless motion generation. Therein, the condition of reactionless motion was derived from the angular momentum conservation law. The method was confirmed ~~at~~ the

on-orbit experiment with ETS-VII [14].

In the previous studies, reactionless motion controls based on RNS have been considered by several researchers [15–17]. For instance, the angular momentum distribution control for capturing non-cooperative satellites under the reactionless condition was proposed [18]. The capability of the method was investigated with a planar model. With a dual arm planar model, point-to-point (PTP) reactionless motion control was considered for capturing space debris [19]. For vibration suppression of flexible appendages on a satellite, reactionless motion control of the end-effector was considered in addition to the vibration suppression control [15]. In these studies, position control of the end-effector under reactionless motion was focused on. However, the position control between arbitrary locations would be impossible on general type of spatial manipulators, e.g. six-DoF and seven-DoF redundant manipulators, due to the limitation of these kinematic structure. In fact, the above methods were verified with planer models only; the possibility with spatial models is uncertain so far.

On spatial manipulators, some interesting studies have been reported. With ETS-VII, simple reactionless tasks was proposed for the on-orbit experiment [14, 20]. In addition, the performance of a modified ETS-VII model added an additional joint was examined. In that study, it was concluded that the mechanisms that have kinematic redundancy is important for extension of the workspace under reactionless motion control. For point-to-point position control, the reaction-null/Jacobian transpose controller, which is a filtered version of the conventional transpose Jacobian controller, was proposed in [21]. This method was verified with spatial serial and dual arm manipulator systems with a six-DoF manipulator. From the result, it was shown that a reachable region of the end-effector from an initial configuration became quite narrow due to the limitation of the structure. This decreasing of the workspace is related to the singularities associated with the reaction-

less constraint and the end-effector position constraint. For this problem, a singularity treatment method named the *singularity consistent* was applied to the singularity within a same type of minimum reaction control. Through this method, unstable behavior near the singularity was able to be avoided. However, it was also confirmed that the workspace became quite narrow.

From this brief overview, we can conclude that position control of the end-effector under reactionless motion control is not applicable in practice due to its small workspace. However, despite the above disadvantage, reactionless motion control can be useful if we plan a motion appropriately. As one of the our research issue, we aim to propose some motion tasks for execution under reactionless motion control.

1.1.3 Energy consumption

As a different issue in space systems, energy consumption have been considered. In the case of controlling satellite attitude, a power minimization control with redundant reaction wheels were proposed in [22]. From the perspective of tool design, a low-power image payload was discussed [23, 24]. In that study, Control Moment Gyros (CMG) were employed because its mechanical power/energy is smaller than these produced by a reaction wheel assembly.

On the other hand, in the field of robotics, a control method that reduces the energy consumption of free-flying space robots was proposed [25]. The study assumed that the base attitude is controlled through four reaction wheels. Then, the redundant reaction wheel was used to reduce the energy consumption throughout a manipulator motion. In [26], the mechanical power was used as a cost function that is to be minimized.

On reactionless motion control, the energy optimum reactionless path planning was proposed [27]. The method utilized redundancy to optimize the kinetic energy of dual manipulators. However, a rapid change of the joint

velocities was observed due to the optimization.

As mentioned in [23], reaction wheels require high amount of mechanical power when a large output torque is generated. Generally, when reaction wheels are used to compensate the base reaction induced by a manipulator motion, the reaction wheels must generate a high output torque. Consequently, the energy consumption becomes large. On the other hand, reactionless motion control need not use reaction wheels completely. Hence, it is possible to reduce the energy consumption without an additional optimization that usually induces unstable behaviors. The reduction of the energy consumption when using reactionless motion control has not been discussed before. In this work, we focus on the energy consumption reduction and show an interesting result.

1.2 Motion/Force control

On terrestrial robots, force control of the end-effector is as important as motion control. Especially under interaction tasks, whose typical examples are polishing, deburring, machining or assembly in industrial settings, force control is crucial due to safe contact between the end-effector of a manipulator and the surfaces. Force control schemes can be divided into impedance control and hybrid motion/force control.

=====

Editing...

=====

1.3 Aim of this study

This thesis treats the following two topics for the RNS-based controls: (i) reactionless motion control for free-floating space robots and (ii) motion/force

control for redundant manipulators.

On reactionless motion control of free-floating space robots, we discuss the following issues:

- i-1** Analysis of reactionless motion from the perspective of nonlinear dynamics.
- i-2** Proposal of some practical tasks suitable for execution under reactionless motion control.
- i-3** Analysis of the energy consumption under reactionless motion control.

On the RNS-based motion/force control, we treat the following topics:

- ii-1** Obtain a specific modeling for the RNS-based motion/force control.
- ii-3** Clarify the joint motion under the RNS-based motion/force control.

1.4 Outline of this thesis

This thesis consists of ~~the~~ eight chapters as follows: Chapter 2 describes the modeling of free-floating base robot systems. The equation of motion of the system is derived from the Euler-Lagrange's equation. Then, linear and angular momentum conservation laws are derived via considering the invariance of the system Lagrangian ~~with~~ translation and rotation of the entire system. Finally, we present the Reaction Null-Space formulation with dimensions of both velocity and acceleration.

In Chapter 3 to 5, we deal with reactionless motion control of free-floating space robots. In Chapter 3, we provide an analysis of reactionless motion with a planar two-DoF model from the perspective of nonlinear dynamics: vector field, fixed point and bifurcation. Besides, with a seven-DoF redundant manipulator, we obtain a representation of its reactionless motion that is useful to consider practical reactionless tasks.

Chapter 4 discusses motion tasks suitable for execution under reactionless motion control. We propose the following three tasks: (i) inspection task using a hand camera, (ii) point-to-point positioning task, (iii) deployment task from a stowed configuration. The performance of these tasks are verified via numerical simulations.

In Chapter 5, we deal with the energy consumption of free-flying space robots, comparing that produced by reactionless motion control with that produce by reaction wheels used controllers. Under zero base attitude deviation, we show that reactionless motion highly coincides with the instantaneous energy minimum motion. Then, the energy consumption of reactionless motion control is compared with a conventional controller using reaction wheels under the inspection tasks.

In the next two chapters, we deal with ~~a~~ motion/force control based on Reaction Null-Space for redundant manipulators. In Chapter 6, we formulate the RNS-based motion/force control. Then, the modeling for the RNS-based controller is presented. Finally, the performance of the proposed method is verified via numerical simulations.

Chapter 7 discusses the joint motion under the RNS-based motion/force control. We show an interesting fact that the joint motion under the RNS-based controller is equivalent to that under the resolved acceleration control. ~~The theoretical interpolation and numerical verification are obtained,~~ then.

Finally, Chapter 8 summarizes the thesis.

1.5 The roles of variable's index

Basically, we describe vectors and matrices according to the following roles of index. *Left superscript*: reference frames in which quantities are described. *Right superscript*: conditions of variables, e.g. T (Transposed), -1 (Inversion), *des* (Desired), *ref* (Reference) and so on. *Right subscript* physical

quantities, component, manipulator mechanisms and so on.

We provide two examples according to the above roles, in what follows. First, we consider the Jacobian \mathbf{J} associated with end-effector linear velocity \mathbf{v}_e with respect to the inertial coordinate frame $\{I\}$. This matrix is written as ${}^I\mathbf{J}_{v_e}$.

Next, we consider the same Jacobian but it just consists of the positioning subchain P , which is a specific part of a manipulator mechanism. This matrix is written as ${}^I\mathbf{J}_{Pv_e}$. Note that if we consider the whole mechanism of a manipulator, we omit this notation. And also note that the notation of the inertial coordinate frame is omitted below.

Chapter 2

Basic Notation

In this section, we describe the equation of motion of a free-floating base robot. We derive the equation through the Euler-Lagrange's equation. Then, we show that the linear/angular conservation laws, which play an important role in robotics, can be derived from the equation of motion assuming invariance of the system Lagrangian under translation and rotation of the entire system. From linear/angular momentum conservation laws, we formulate the Reaction Null-Space based control method. This formulation is useful for reactionless motion control of space robots and also motion/force control of redundant manipulators.

2.1 Modeling of free-floating base robots

We consider a free-floating base robot that consists of a floating base and links, e.g. manipulators and reaction wheels, as shown in Fig. 2.1. Let us define the inertial coordinate frame $\{I\}$. We use two kind of position vector. One of them is vector from the inertial frame; the other is one from the base coordinate frame $\{B\}$. Note that, except special cases these vectors are described with respect to the inertial frame.

Here, we introduce generalized coordinate to describe the system dynamics.

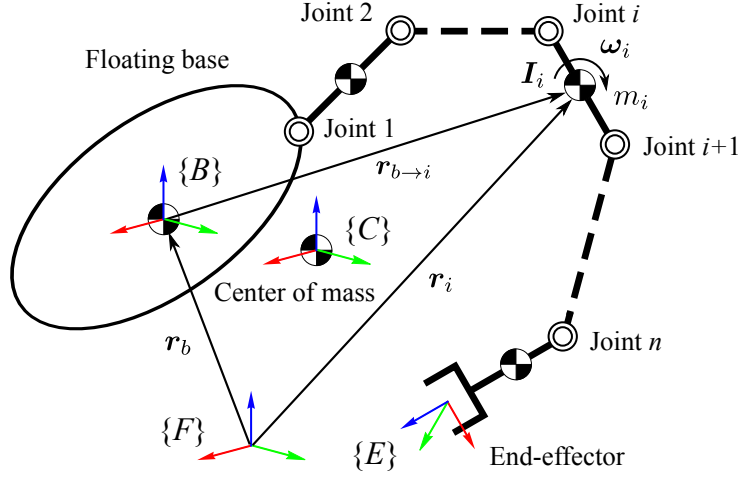


Fig. 2.1: General model of free-floating base robot.

The coordinate is defined as $\mathbf{q} = [\mathcal{X}_b^T \boldsymbol{\theta}^T]^T \in \mathbb{R}^{n+6}$, where $\mathcal{X}_b = [\mathbf{r}_b^T \boldsymbol{\xi}_b^T]^T \in \mathbb{R}^6$ stands for the base variables: $\mathbf{r}_b \in \mathbb{R}^3$ and $\boldsymbol{\xi}_b$ are base position vector and Euler angle describing the base attitude. $\boldsymbol{\theta} \in \mathbb{R}^n$ is the joint variable vector.

2.1.1 Kinematics

Seen from Fig. 2.1, the position vector of each link can be written as follows:

$$\mathbf{r}_i = \mathbf{r}_b + \mathbf{r}_{b \rightarrow i} \quad (2.1)$$

where \mathbf{r}_i , $\mathbf{r}_{b \rightarrow i}$ are the position vectors pointing the center of mass of each link from the inertial frame and the base frame. Differentiating (2.1) with respect to time t , we can obtain the differential kinematic equation:

$$\mathbf{v}_i = \mathbf{v}_b + \mathbf{J}_{v_i}(\mathbf{q})\dot{\boldsymbol{\theta}} + \boldsymbol{\omega}_b^\times \mathbf{r}_{b \rightarrow i} \quad (2.2)$$

where \mathbf{v}_i stands for linear velocity of link i , \mathbf{v}_b , $\boldsymbol{\omega}_b \in \mathbb{R}^3$ are linear and angular velocities of the base. $\mathbf{J}_{v_i}(\mathbf{q}) \in \mathbb{R}^{3 \times n}$ is the Jacobian of linear velocity of link i . $(\dot{\circ})$ and $(\circ)^\times$ define time differential and skew-symmetric matrix.

In contrast to the linear velocity equation, the kinematic equation of angular velocity cannot be obtained directly as the time differential of the position-level equation because its non-integrability. Angular velocity of link i is expressed in the following form:

$$\boldsymbol{\omega}_i = \boldsymbol{\omega}_b + \mathbf{J}_{\omega_i}(\mathbf{q})\dot{\boldsymbol{\theta}} \quad (2.3)$$

where $\boldsymbol{\omega}_i$ stands for angular velocity of link i , $\mathbf{J}_{\omega_i}(\mathbf{q}) \in \mathbb{R}^{3 \times n}$ is the Jacobian associated with the angular velocity of link i .

For description convenience, we introduce twist vector $\mathcal{V}_i = [\mathbf{v}_i^T \ \boldsymbol{\omega}_i^T]^T$. By using this notation, the generalized velocity vector can be written as $\dot{\mathbf{q}} = [\mathcal{V}_b^T \ \dot{\boldsymbol{\theta}}^T]^T$, hereafter.

2.1.2 Kinetic energy

The kinetic energy of the link mechanism is represented in the following form:

$$T = \frac{1}{2} \sum_{i=0}^n (m_i \mathbf{v}_i^T \mathbf{v}_i + \boldsymbol{\omega}_i^T \mathbf{I}_i \boldsymbol{\omega}_i) \quad (2.4)$$

where T is kinetic energy, m_i and $\mathbf{I}_i \in \mathbb{R}^3$ are the mass and the inertia tensor of each link. Substituting (2.2) and (2.3) into the above equation, we can rewrite the kinetic energy in terms of the base and joint variables as follows:

$$T = \frac{1}{2} \dot{\mathbf{q}}^T \mathbf{M}(\mathbf{q}) \dot{\mathbf{q}} \quad (2.5)$$

$$= \frac{1}{2} [\mathcal{V}_b^T \ \dot{\boldsymbol{\theta}}^T] \begin{bmatrix} \mathbf{M}_b(\mathbf{q}) & \mathbf{M}_{bl}(\mathbf{q}) \\ \mathbf{M}_{bl}(\mathbf{q})^T & \mathbf{M}_l(\mathbf{q}) \end{bmatrix} \begin{bmatrix} \mathcal{V}_b \\ \dot{\boldsymbol{\theta}} \end{bmatrix} \quad (2.6)$$

where $\mathbf{M}(\mathbf{q}) \in \mathbb{R}^{(n+6) \times (n+6)}$ is the inertia matrix of the entire mechanism. $\mathbf{M}_b(\mathbf{q}) \in \mathbb{R}^{6 \times 6}$, $\mathbf{M}_{bl}(\mathbf{q}) \in \mathbb{R}^{6 \times n}$ and $\mathbf{M}_l(\mathbf{q}) \in \mathbb{R}^{n \times n}$ are the submatrices of the inertia matrix. Especially \mathbf{M}_b is the inertia matrix of the system regarded as a Composite-Rigid-Body (CRB), \mathbf{M}_{bl} is a block sumatrix of the system inertia matrix. This matrix represents a coupling between base motion and

link motion. Hence, it has been referred to as the *coupling inertia* matrix, and plays an important role under controlling space robots. Finally, \mathbf{M}_l is so-called the manipulator inertia matrix.

2.1.3 Inertia submatrices

Here, we provide the definition of the inertia submatrices described the above.

The base inertia matrix \mathbf{M}_b is defined in the following form:

$$\mathbf{M}_b = \begin{bmatrix} \mathbf{M}_v & \mathbf{M}_{v\omega} \\ \mathbf{M}_{v\omega}^T & \mathbf{M}_\omega \end{bmatrix} \quad (2.7)$$

$$\mathbf{M}_v = m_{com} \mathbf{E} \quad (2.8)$$

$$\mathbf{M}_{v\omega} = - \sum_{i=0, i \neq b}^n m_i \mathbf{r}_{b \rightarrow i}^\times \quad (2.9)$$

$$\mathbf{M}_\omega = \sum_{i=0, i \neq b}^n (\mathbf{I}_i - m_i \mathbf{r}_{b \rightarrow i}^\times \mathbf{r}_{b \rightarrow i}^\times) + \mathbf{I}_b \quad (2.10)$$

where $m_{com} = \sum_{i=0}^n m_i$ is the total mass of the system, m_i and $\mathbf{I}_i \in \mathbb{R}^3$ is the mass and the inertia tensor of link i . $\mathbf{E} \in \mathbb{R}^{3 \times 3}$ is the identity matrix.

The coupling inertia matrix \mathbf{M}_{bl} is defined as follows:

$$\mathbf{M}_{bl} = \begin{bmatrix} \mathbf{M}_{vl} \\ \mathbf{M}_{\omega l} \end{bmatrix} \quad (2.11)$$

$$\mathbf{M}_{vl} = \sum_{i=0, i \neq b}^n m_i \mathbf{J}_{v_i} = m_{com} \mathbf{J}_{com} \quad (2.12)$$

$$\mathbf{M}_{\omega l} = \sum_{i=0, i \neq b}^n (\mathbf{I}_i \mathbf{J}_{\omega_i} + m_i \mathbf{r}_{b \rightarrow i}^\times \mathbf{J}_{v_i}) \quad (2.13)$$

where $\mathbf{J}_{com} \in \mathbb{R}^{3 \times n}$ is the Jacobian matrix with respect to the CoM velocity of the system; hence it is referred to as the CoM Jacobian.

Finally, \mathbf{M}_l is as follows:

$$\mathbf{M}_l = \sum_{i=1}^n (m_i \mathbf{J}_{v_i}^T \mathbf{J}_{v_i} + \mathbf{J}_{\omega_i}^T \mathbf{I}_i \mathbf{J}_{\omega_i}) \quad (2.14)$$

Note that this matrix is the same as the manipulator inertia matrix of fixed base robots.

2.1.4 Equation of motion

Since we consider free-floating systems, the gravity potential is approximately zero. Hence, the system Lagrangian coincides with the kinetic energy:

$$L(\mathbf{q}, \dot{\mathbf{q}}) = T(\mathbf{q}, \dot{\mathbf{q}}) \quad (2.15)$$

where $L(\mathbf{q}, \dot{\mathbf{q}})$ is the system Lagrangian.

From the theory of analytical mechanics, equation of motions of dynamic system can be obtained through partial derivation of the system Lagrangian. Then, equation of motions satisfy the following equation:

$$\frac{d}{dt} \left(\frac{\partial L}{\partial \dot{\mathbf{q}}} \right) - \frac{\partial L}{\partial \mathbf{q}} = \mathbf{Q} \quad (2.16)$$

where \mathbf{Q} is generalized force vector acting on each generalized coordinate.

Substituting (2.6) and (2.15) into (2.16), we can obtain the equation of motion of a free-floating base robot in the following form:

$$\mathbf{M}_b \dot{\mathbf{V}}_b + \mathbf{M}_{bl} \ddot{\boldsymbol{\theta}} + \mathbf{C}_b = \mathbf{0} \quad (2.17)$$

$$\mathbf{M}_{bl}^T \dot{\mathbf{V}}_b + \mathbf{M}_l \ddot{\boldsymbol{\theta}} + \mathbf{c}_l = \boldsymbol{\tau} \quad (2.18)$$

where $\boldsymbol{\tau} \in \mathbb{R}^n$ is joint torque acting on each joint, $\mathbf{C}_b \in \mathbb{R}^6$ and $\mathbf{c}_l \in \mathbb{R}^n$ are nonlinear dependent force of the base and the links. These nonlinear force are represented in the following form:

$$\mathbf{c} = \begin{bmatrix} \mathbf{C}_b \\ \mathbf{c}_l \end{bmatrix} = \dot{\mathbf{M}} \dot{\boldsymbol{\theta}} - \frac{1}{2} \frac{\partial}{\partial \mathbf{q}} \left(\dot{\mathbf{q}}^T \mathbf{M} \dot{\mathbf{q}} \right) \quad (2.19)$$

Equation (2.17) represents the dynamics of the composite rigid-body (CRB); (2.18) describes the same dynamics with respect to the local coordinate frames attached on each joint.

2.2 Momentum conservation law

2.2.1 Linear momentum conservation law

In the field of robotics, linear and angular momenta and their conservation laws play an important role. In particular, these provide the reactionless motion constraint on space robots. In the field of humanoids, these are used to build balancing controllers and also whole body motion controllers. Considering the invariance of the system Lagrangian under variations of position and rotation of a dynamic system, we can obtain the conservation laws in what follows.

First, we derive the linear momentum conservation law of free-floating base robots. Empirically, we know that physical laws do not change with translation of dynamic systems; the translation indicates that the whole part of the system move for a same direction, simultaneously.

We assume that the system consists of n bodies like manipulator mechanisms. Among the generalized coordinates, the position vectors pointing to each body are defined as \mathbf{r}_i . Then, under a variation of translation $\delta\mathbf{r}_i$, the variation of the system Lagrangian can be written as follows:

$$\delta L = \sum_{i=1}^n \frac{\partial L}{\partial \mathbf{r}_i} \delta \mathbf{r}_i \quad (2.20)$$

Because the variation of the Lagrangian must be zero with an arbitrary value of $\delta\mathbf{r}_i$, the following condition must satisfy:

$$\sum_{i=1}^n \frac{\partial L}{\partial \mathbf{r}_i} = \mathbf{0} \quad (2.21)$$

According to (2.16), the above condition is equivalent to the following equation:

$$\sum_{i=1}^n \frac{d}{dt} \left(\frac{\partial L}{\partial \dot{\mathbf{r}}_i} \right) = \mathbf{0} \quad (2.22)$$

where $\sum \frac{\partial L}{\partial \dot{\mathbf{r}}_i}$ is an invariable and $\mathbf{p}_i = \frac{\partial L}{\partial \dot{\mathbf{r}}_i}$ is defined as *linear momentum*. Hence, (2.22) represents linear momentum conservation law. Using the expression of (2.4), the conservation law can be written in the following well-known form:

$$\mathbf{p} = \sum_{i=1}^n m_i \mathbf{v}_i \quad (2.23)$$

In the case of free-floating base robots, a variation of translation can be considered as the base position vector $\delta \mathbf{r}_b$. Then, the linear momentum conservation law of free-floating base robots can be obtained as:

$$\frac{d}{dt} \left(\frac{\partial L}{\partial \mathbf{v}_b} \right) = \mathbf{0} \quad (2.24)$$

This is equivalent to the following equation:

$$\mathbf{p} = \mathbf{M}_v \mathbf{v}_b + \mathbf{M}_{v\omega} \boldsymbol{\omega}_b + \mathbf{M}_{vl} \dot{\boldsymbol{\theta}} \quad (2.25)$$

The above expression of the conservation law has been used in various studies.

2.2.2 Angular momentum conservation law

We derive the angular momentum conservation law of free-floating base robots. In contrast to linear momentum conservation law, angular momentum conservation law is obtained from invariance of the system Lagrangian under an infinitesimal rotation of dynamic systems.

First, we derive, also, the general form of angular momentum conservation law. We introduce an infinitesimal rotation vector $\delta \boldsymbol{\psi}$. Then, a position vector pointing to an arbitrary particle of a rotating system varies according to $\delta \boldsymbol{\psi}$. The position variation is written as follows (see Fig. 2.2):

$$\|\delta \mathbf{r}\| = r \sin \alpha \|\delta \boldsymbol{\psi}\| \quad (2.26)$$

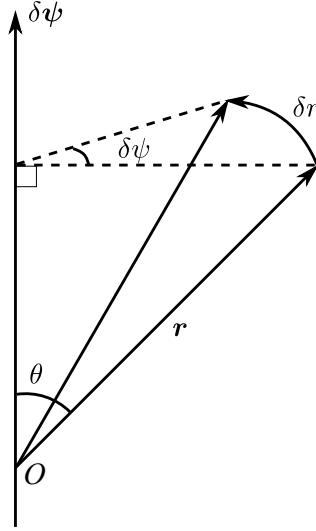


Fig. 2.2: Relationship between a variation of translation and a rotational variation.

Under an arbitrary infinitesimal rotation, velocity of each body also varies. The variation of the velocity is written as:

$$\delta \mathbf{v} = \delta \boldsymbol{\psi} \times \mathbf{v} \quad (2.27)$$

With the above relation, the variation of the system Lagrangian under an infinitesimal rotation can be written as:

$$\begin{aligned} \delta L &= \sum \left\{ \dot{\mathbf{p}}_i (\delta \boldsymbol{\psi}^T \mathbf{r}_i) + \mathbf{p}_i (\delta \boldsymbol{\psi}^T \mathbf{v}_i) \right\} \\ &= \delta \boldsymbol{\psi} \frac{d}{dt} \sum_i \mathbf{r}_i \times \mathbf{p}_i \\ &= 0 \end{aligned} \quad (2.28)$$

Because $\delta \boldsymbol{\psi}$ can be an arbitrary value, the following condition must satisfy:

$$\frac{d}{dt} \sum \mathbf{r}_i \times \mathbf{p}_i = \mathbf{0} \quad (2.29)$$

Hence, we found out that the quantity $\sum \mathbf{r}_i \times \mathbf{p}_i$ conserves; $\mathbf{l}_i = \mathbf{r}_i \times \mathbf{p}_i$ is defined as *angular momentum*. Using the same expression of (2.4), we can rewrite the angular momentum conservation law in the following form:

$$\mathbf{l} = \sum_i^n \left\{ \mathbf{I}_i \boldsymbol{\omega}_i + m_i \mathbf{r}_i \times \mathbf{v}_i \right\} \quad (2.30)$$

In the case of free-floating robots, this equation is the same as follows:

$$\mathbf{l} = \mathbf{M}_{v\omega}^T \mathbf{v}_i + \mathbf{M}_\omega \boldsymbol{\omega}_b + \mathbf{M}_{\omega l} \dot{\boldsymbol{\theta}} + \mathbf{r}_b \times \mathbf{p} \quad (2.31)$$

2.3 Reaction Null-Space

Reaction Null-Space was originally proposed for reactionless motion control of space robots. On the experience with ETS-VII, the possibility of reactionless motion control was confirmed. Here, we describe the Reaction Null-Space formulation with dimensions of both momentum and dynamics.

2.3.1 Momentum based derivation

First, we explain the momentum based formulation. The spatial momentum conservation law is obtained in the following form:

$$\mathcal{L} = \mathbf{M}_b \mathcal{V}_b + \mathbf{M}_{bl} \dot{\boldsymbol{\theta}} \quad (2.32)$$

where $\mathcal{L} = [\mathbf{p}^T \mathbf{l}_b^T]^T$ is spatial momentum. From the above equation, we confirm that there are two partial momenta: $\mathbf{M}_b \mathcal{V}_b$ represents the partial momentum related to base motion; $\mathbf{M}_{bl} \dot{\boldsymbol{\theta}}$ is stemming from manipulator motion. In particular, the later one has been referred to as the *coupling momentum*, and is characterized by the coupling inertia matrix.

Solving (2.32) for joint velocity, we can obtain a joint-space decomposition in terms of the dynamics coupling as follows:

$$\dot{\boldsymbol{\theta}} = \mathbf{M}_{bl}^+ (\mathcal{L} - \mathbf{M}_b \mathcal{V}_b) + \mathbf{P}_{RNS} \dot{\boldsymbol{\theta}}_a \quad (2.33)$$

where $(\circ)^+$ defines pseudoinverse matrix, $\mathbf{P}_{RNS} = \mathbf{E} - \mathbf{M}_{bl}^+ \mathbf{M}_{bl} \in \mathbb{R}^{n \times n}$ is the projector onto the null-space of the coupling inertia matrix. $\dot{\boldsymbol{\theta}}_a \in \mathbb{R}^n$ is an arbitrary vector with dimensions of joint velocity. The first term represents joint velocities inducing a base motion; on the other hand, the second term does not impose any motion at the base. Hence, the motions are referred to as *reactionless motion*. Since the property of pseudoinverse, the above two terms are orthogonal with any values of $(\mathcal{L} - \mathbf{M}_b \mathcal{V}_b)$ and $\dot{\boldsymbol{\theta}}_a$. This joint space decomposition has been referred to as *Reaction Null-Space* with dimensions of momentum.

2.3.2 Dynamics based derivation

Let us recall the equation of motion (2.17), as follows:

$$\mathbf{M}_b \dot{\mathcal{V}}_b + \mathbf{M}_{bl} \ddot{\boldsymbol{\theta}} + \mathcal{C}_b = \mathbf{0} \quad (2.34)$$

From the above equation, we can also see that there is a coupling between the base dynamics and the manipulator one through the coupling inertia matrix. Through the same approach under the momentum-based derivation, the Joint dynamics can be divided into two parts in the following form:

$$\ddot{\boldsymbol{\theta}} = \mathbf{M}_{bl}^+ (\mathbf{M}_b \dot{\mathcal{V}}_b - \mathcal{C}_b) + \mathbf{P}_{RNS} \dot{\boldsymbol{\theta}}_a \quad (2.35)$$

The first term on the r.h.s. represents joint accelerations inducing a base motion, the second term defines reactionless acceleration, whose meaning is the same as the momentum derivation. Note that the motions of (2.33) and (2.35) are not basically equivalent, since there is no integrability between the two formulations; this non-integrability is due to the pseudoinverse.

2.4 Summary

In this section, we describe the equation of motion of a free-floating base robots from the Euler-Lagrange formulation. We show the two important

conservation law, which are linear and angular momentum conservation law, with assuming invariance of the system Lagrangian under variation of position and orientation of dynamic systems. Then, we derive the Reaction Null-Space formulation with dimensions of both momentum and dynamics. Joint velocity/acceleration can be divided into two parts through the inertia coupling matrix. The first part is a motion set inducing a base motion, the second part does not effect a base motion. Hence, the second one is referred to as reactionless motion. Based on this formulation, we describe reactionless motion of a free-floating space manipulator and motion/force control for redundant manipulators, below.

Chapter 3

Review of Reactionless Motion and Analysis

3.1 Reactionless motion control

Motion of a free-floating space robot is described via the spatial momentum conservation law as follows:

$$\begin{bmatrix} \mathbf{p} \\ \mathbf{l}_b \end{bmatrix} = \begin{bmatrix} \mathbf{M}_v & \mathbf{M}_{v\omega} \\ \mathbf{M}_{v\omega}^T & \mathbf{M}_\omega \end{bmatrix} \begin{bmatrix} \mathbf{v}_b \\ \boldsymbol{\omega}_b \end{bmatrix} + \begin{bmatrix} \mathbf{M}_{vm} \\ \mathbf{M}_{\omega m} \end{bmatrix} \dot{\boldsymbol{\theta}} + \begin{bmatrix} \mathbf{0} \\ \mathbf{r}_b \times \mathbf{p} \end{bmatrix} \quad (3.1)$$

In this case, the link part is actually a manipulator. Hence, we use the subscript $(\circ)_m$ to represent “manipulator”.

On free-floating space robots, base rotation is a problem due to the communication between the satellite and the ground control center. Hence, the angular momentum conservation law that describes behavior of base rotation is more important than the linear one. Solving the upper part of (3.1) for base linear velocity and substituting it into the lower part of (3.1), we can obtain the angular momentum conservation law in the following form:

$$\mathbf{l}_b = \tilde{\mathbf{M}}_\omega \boldsymbol{\omega}_b + \tilde{\mathbf{M}}_{\omega m} \dot{\boldsymbol{\theta}} \quad (3.2)$$

where $\tilde{\mathbf{M}}_\omega = \mathbf{M}_\omega - \mathbf{M}_{v\omega}^T \mathbf{M}_v^{-1} \mathbf{M}_{v\omega}$ and $\tilde{\mathbf{M}}_{\omega m} = \mathbf{M}_{\omega m} - \mathbf{M}_{v\omega}^T \mathbf{M}_v \mathbf{M}_{vm}$. The notation $(\tilde{\circ})$ represents the matrices that include base linear motion. In the

above equation, the second term represents the base reaction induced by a manipulator motion with dimensions of momentum.

To deal with the reaction problem, reactionless motion control can be a useful approach. Reactionless motions are variations of the manipulator configuration that conserve a zero initial base angular momentum throughout a manipulator motion. As explained already in Chapter 2, these motions are obtained from the null-space vectors of the coupling inertia matrix. Then, reactionless motion velocities are obtained as:

$$\dot{\boldsymbol{\theta}} = \mathbf{P}_{RNS} \dot{\boldsymbol{\theta}}_a \quad (3.3)$$

The velocities, of course, satisfy the following equation:

$$\tilde{\mathbf{M}}_{\omega m} \dot{\boldsymbol{\theta}} = \mathbf{0} \quad (3.4)$$

The above equation implies the reactionless constraint.

Because $\dot{\boldsymbol{\theta}}_a$ is projected into $\ker(\tilde{\mathbf{M}}_{\omega m})$, any values of $\dot{\boldsymbol{\theta}}_a$ satisfy the reactionless constraint (3.4). The main concern of this study is how to make use of reactionless motions in practice. Before proceeding with the discussion of the practical use, we should discuss the features of reactionless motion. This section provides an analysis on reactionless motion with a planar model.

3.2 Qualitative study of reactionless motion

Despite reactionless motion control has been considered in several studies, the characters of reactionless motion have not been discussed so far. Let us consider a planar two-DoF manipulator as shown in Fig. 3.1. This model is the most simplest model that can generate reactionless motion. Reactionless motion of this model can be represented as follows:

$$\dot{\boldsymbol{\theta}} = b\mathbf{n}(\boldsymbol{\theta}) \quad (3.5)$$

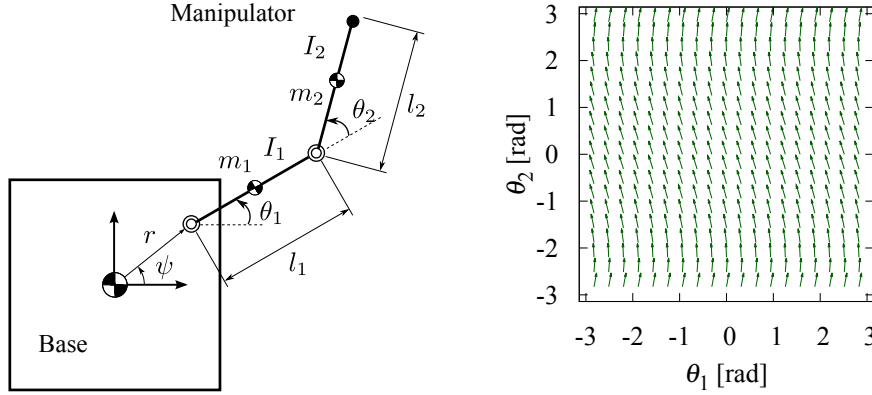


Fig. 3.1: A planer two-DoF space manipulator model, whose parameters are $m_i = 100$ kg, $l_i = 1.0$ m ($i = 1, 2$); the base mass is $m_b = 1000$ kg, and its reactionless motion vector field.

where $\mathbf{n}(\boldsymbol{\theta}) \in \mathbb{R}^2$ is the null-space vector of the coupling inertia matrix, b is an arbitrary scalar. $\mathbf{n}(\boldsymbol{\theta})$ can be uniquely obtained through appropriate methods, i.e. Singular Value Decomposition (SVD) or co-factor method. We assume that $\mathbf{n}(\boldsymbol{\theta})$ is already normalized, and b is a time-independent constant scalar, for the sake of simplicity. Hence, (3.5) can be regarded as an autonomous nonlinear system. The right hand side in (3.5) defines the vector field of reactionless motion on the joint space.

We examine the characters of reactionless motion with the vector field of the above system. For the sake of simplicity, we assume that the manipulator is attached on the CoM of the base. The masses are $m_b = 1000$ kg, $m_1 = m_2 = 100$ kg, and the link length are $l_1 = l_2 = 1.0$ m, respectively. Then, the vector field is depicted in Fig. 3.1.

Because the manipulator is attached symmetrically, the vector field has rotational symmetry with respect to joint 1. As an important character, we can see that the reactionless motion almost consists of the motion of joint 2. Because reactionless motion is a motion that conserves the angular momentum to zero (or constant), joints that induce a large angular momentum

cannot move widely. In this case, the angular momentum induced by the motions of joint 1 must be larger than that induced by the motions of joint 2 due to the large inertia moment and the long moment arm. As a result, the above mentioned character was observed.

3.2.1 Fixed point and bifurcation

In the above case, there is no fixed point in the system. However, with variation of a specific parameter, we can observe the creation of the fixed points on reactionless motion. This bifurcation phenomenon largely depends on the manipulator attachment position. We define the attachment position in the following form:

$$\begin{bmatrix} x_a \\ y_a \end{bmatrix} = r \begin{bmatrix} \cos \psi \\ \sin \psi \end{bmatrix} \quad (3.6)$$

where $(\circ)_a$ is the coordinate of the attachment position, r is the distance between the attachment position and the base CoM, ψ is the angle that is shown in Fig. 3.1. Among these parameters, r plays an important role as a *bifurcation parameter*. Note that we will assume $\psi = 0$ rad because this parameter does not influence the topological structure of the system due to the rotational symmetry of mechanics. The condition $\psi = 0$ rad implies that the manipulator attachment position varies along x -axis of the base frame.

We show the vector field and nullclines with several values of r in Fig. 3.2. In the figures, the upper part represents the vector fields and the lower part depicts nullclines for each joint: the lines in red are nullclines for joint 1, the lines in blue are these for joint 2. When $r = 0.5$ m, we can see that there is no fixed point, because the motion of joint 2 never stops at any points on joint space. On the other hand, the occurrence of bifurcation can be observed when $r \approx 0.945$ m. Then, two fixed points are created at the points where two nullclines intersect. By increasing the bifurcation parameter, it is observed that the additional two fixed points are created ($r = 1.5$ m). Summary, we

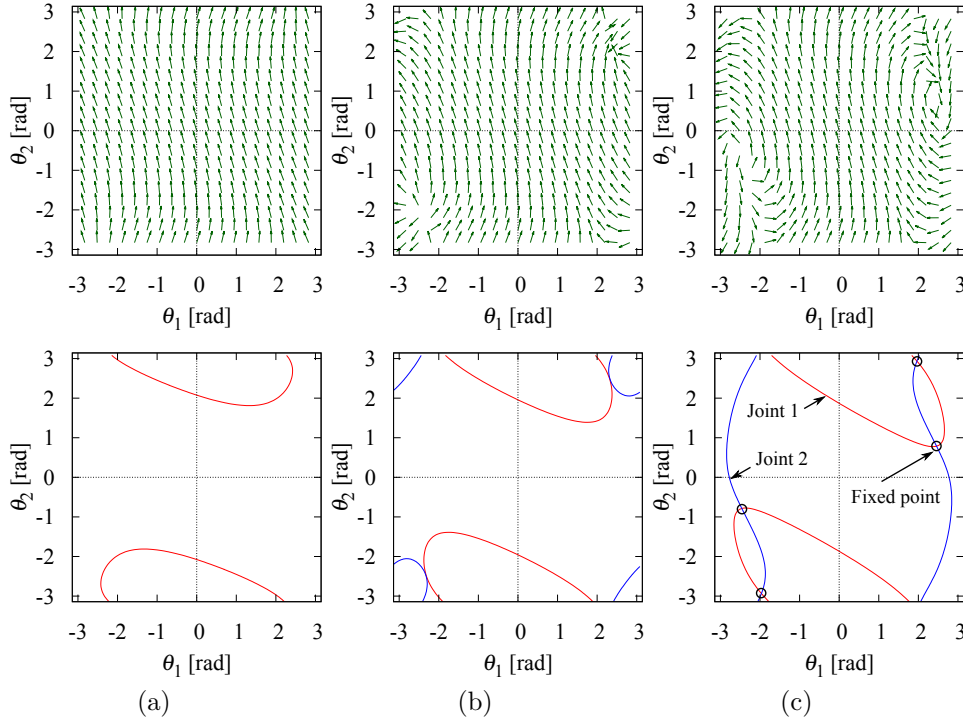


Fig. 3.2: The vector field and nullclines for each joint direction with variation r : (a) $r = 0.5$ m, (b) $r = 0.945$ m and (c) $r = 1.5$ m.

can confirm that the manipulator attachment position play the important role on reactionless motion.

3.2.2 Details of the fixed point

In the above discussion, we showed the existence of the fixed point of reactionless motion control. This is related to the singularities of the coupling inertia matrix. We provide an insight of the singularity with the planar model mentioned above.

We show the determinant of the coupling inertia matrix with $r = 1.5$ m as a color map in Fig. 3.3 (a). In the color map, the determinant takes large values in bright areas, while the most dark area represents the singularity.

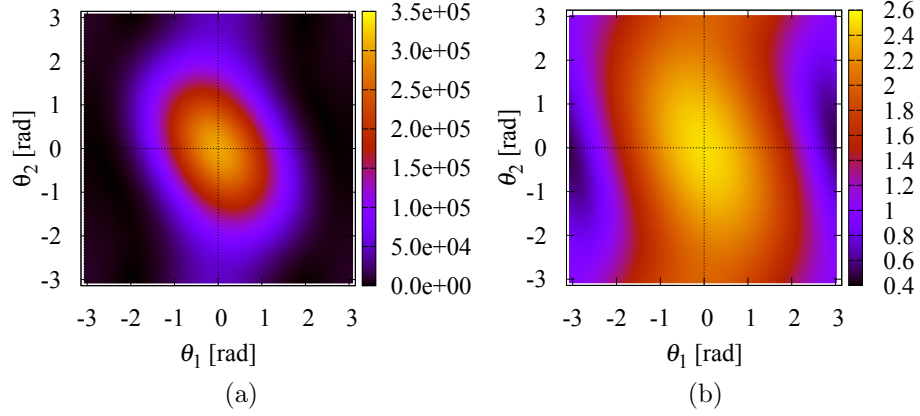


Fig. 3.3: This figure shows the determinant of the coupling inertia matrix and the distance between the manipulator CoM and the base one as color map: (a) $\det(\tilde{\mathbf{M}}_{wm} \tilde{\mathbf{M}}_{wm})$ and (b) the distance between the manipulator CoM and the base one.

We can see that the determinant takes its maximum value at $\boldsymbol{\theta} = [0 \ 0]^T$ rad. This is an extended configuration and the manipulator CoM is located on the farthest away from the base CoM with this configuration. The amplitude of the determinant can be related to the distance between the manipulator CoM and the base one, because the distance determines the amplitude of the coupling angular momentum. The distance is depicted on the joint space as Fig. 3.3 (b). Comparing these maps, we can see that the determinant takes large values when the distance is long: there is no fixed point within the location where the CoM distance becomes large. However, if we consider spatial models, the direction of each joint axis also can be related to the determinant. The analysis with spatial models would be a future work.

3.3 Summary

In this chapter, we described some characters of reactionless motion with a planar model. From a qualitative analysis, we found out that the manipulator

attachment position plays an important role in terms of bifurcation. Then, through vector field, we confirmed that the fixed points of reactionless motion are generated, increasing the length between the manipulator attachment position and the base CoM.

Chapter 4

Proposal of Reactionless Tasks

In this chapter, we discuss motion tasks suitable for execution under reactionless motion control, with a seven-DoF redundant manipulator. The reactionless motion of the model consists of the predominant wrist and elbow motion. Based on these motions, we propose the following three tasks [28]: (i) inspection task using a hand camera, (ii) point-to-point position control, (iii) deployment task from a stowed configuration. The performance of these tasks are verified via numerical simulation.

4.1 Manipulator model

4.1.1 Model description

In the practical use of reactionless motion control, we consider a free-flying space robot model consisting of a satellite base and a serial seven-DoF redundant manipulator as shown in Fig. 4.1. The manipulator is characterized by a kinematic chain with a distinctive lower/upper arm subchain, including a rotational “elbow” joint and “shoulder” and “wrist” joints with offsets. The manipulator attachment position are designed based on that of ETS-VII as $[-0.79 \ -0.29 \ 1.0]^T$ m with respect to the base CoM [5]. The dynamic model parameters are shown in Tab. 4.1.

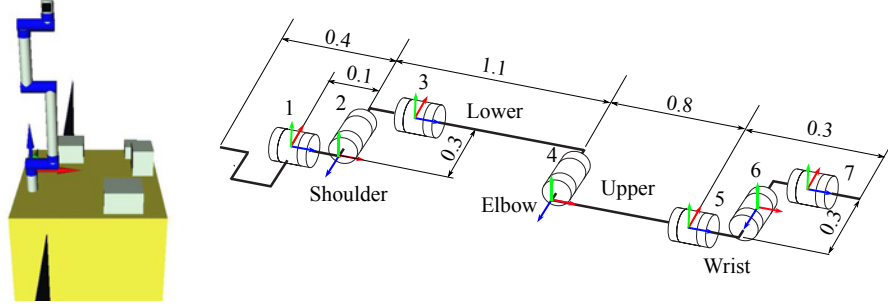


Fig. 4.1: Our manipulator model with seven-DoF mechanism at the initial configuration ($\theta_i = 0 \text{ rad}, \forall \theta_i$).

Table 4.1: Dynamic model parameters

i	Mass [kg]	Inertia moment [kgm ²]		
	m_i	I_{xi}	I_{yi}	I_{zi}
1	30.0	0.0671	0.0671	0.0851
2	30.0	0.0843	0.267	0.267
3	45.0	3.81	3.81	0.127
4	40.0	0.113	2.19	2.19
5	20.0	0.213	0.213	0.0250
6	20.0	0.0250	0.0292	0.0292
7	25.0	0.0990	0.0990	0.0313

4.1.2 Reactionless motion representation

Before proceeding with the proposal of practical reactionless motion task, we have to identify reactionless motion with the manipulator model. In this model, the DoF of reactionless motion is four, which is obtained from the difference between the number of joints and the base attitude DoF (three). The following discussion provides a useful representation of the four-DoF motion. First, we divide the kinematic structure into the positioning and the wrist subchains for practical aspect. The positioning subchain consists

of Joint 1 through 4. The rest of joints constitute the wrist subchain.

Dividing joint velocity into the positioning and wrist subchain related terms, we can rewrite the reactionless constraint as follows:

$$\tilde{\mathbf{M}}_{P\omega m}\dot{\boldsymbol{\theta}}_P + \tilde{\mathbf{M}}_{W\omega m}\dot{\boldsymbol{\theta}}_W = \mathbf{0} \quad (4.1)$$

where $\dot{\boldsymbol{\theta}} = [\dot{\boldsymbol{\theta}}_P \ \dot{\boldsymbol{\theta}}_W]$, $\tilde{\mathbf{M}}_{\omega m} = [\tilde{\mathbf{M}}_{P\omega m} \ \tilde{\mathbf{M}}_{W\omega m}]$; $(\circ)_P$ and $(\circ)_W$ represent the quantities related to the positioning and wrist subchains. In the above equation, the first term is the partial angular momentum produced by the positioning subchain; the second term is stemming from the wrist subchain. We focus on the amplitude of these angular momentum. Because of small mass and the length of moment arm, we can regard that the angular momentum produced by the wrist subchain is far smaller than that produced by the positioning subchain. Hence, the base reaction produced by the wrist subchain can be compensated by the positioning subchain. This represents a part of reactionless motion on the model; it can be obtained as follows:

$$\dot{\boldsymbol{\theta}} = \begin{bmatrix} \mathbf{B}(\boldsymbol{\theta}) \\ \mathbf{E} \end{bmatrix} \dot{\boldsymbol{\theta}}_W \quad (4.2)$$

where $\mathbf{B} = -\tilde{\mathbf{M}}_{P\omega m}^+ \tilde{\mathbf{M}}_{W\omega m} \in \mathbb{R}^{4 \times 3}$ is a linear map from the wrist subchain motion to the positioning subchain motion ensuring the reactionless constraint. We define this reactionless motion as *predominant wrist* motion because it largely consists of wrist subchain motions. The DoF of this motion is three. Hence, the one-DoF reactionless motion still remains.

The remaining reactionless motion is uniquely determined as the null-space vector of $\tilde{\mathbf{M}}_{P\omega m}$ as follows:

$$\dot{\boldsymbol{\theta}} = b \begin{bmatrix} \mathbf{n}(\boldsymbol{\theta}) \\ \mathbf{0} \end{bmatrix} \quad (4.3)$$

where b is an arbitrary scalar. From the angular momentum conservation, we can assume that the above motion almost all consists of motions of joint

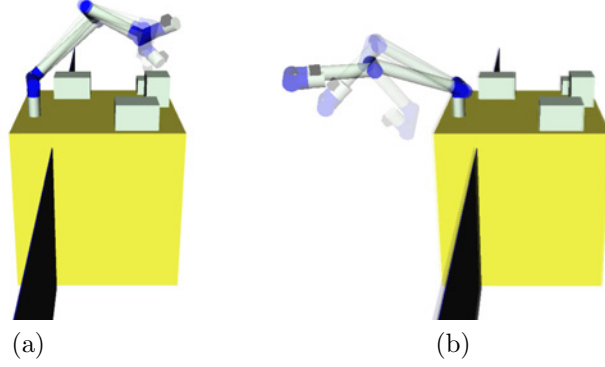


Fig. 4.2: Reactionless motion of the manipulator model: (a) the predominant wrist motion and (b) the elbow folding motion.

3 and 4 because of a small mass/inertia moment related to these motions, as seen in the previous section with the planar model. Hence, this motion approximately consists of elbow motion as shown in Fig. 4.2 (b).

Finally, the whole space of reactionless motion can be covered by the above two motions:

$$\dot{\boldsymbol{\theta}} = \begin{bmatrix} \mathbf{B}(\boldsymbol{\theta}) \\ \mathbf{E} \end{bmatrix} \dot{\boldsymbol{\theta}}_w + b \begin{bmatrix} \mathbf{n}(\boldsymbol{\theta}) \\ \mathbf{0} \end{bmatrix} \quad (4.4)$$

Note that the above two terms are orthogonal because of $\mathbf{B}^T \mathbf{n} = \mathbf{0}$. Hence it is apparent that reactionless motion of the model is represented as superposition of the above two motions.

From the above analysis, we can obtain the following fact: because the end-effector position largely depends on the motion of the positioning subchain, the DoF of end-effector position under reactionless motion is approximately 1 according to that of the positioning subchain. Namely, even if the system has enough DoF, position control under reactionless motion is not feasible due to the limitation of the kinematic structure.

Based on the two type of reactionless motions, we propose the following three tasks for reactionless motion: (i) inspection task using a hand camera,

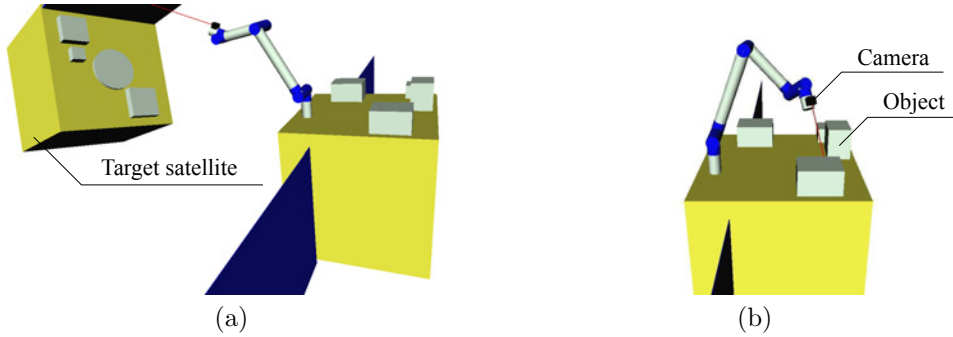


Fig. 4.3: Inspection task using the hand camera: (a) target satellite to be refueled or captured and (b) own-satellite attached devices.

(ii) point-to-point positioning task and (iii) deployment task from a stowed configuration. First, we describe the inspection task in what follows.

4.2 Inspection task using a hand camera

One frequent task for free-floating space robots is inspection with a hand camera for various devices mounted on own satellite, large space structures or satellites to be serviced, as shown in Fig. 4.3. Such task was also performed within the ETS-VII mission [2] without using reactionless control. At this motion task, once the arm is positioned appropriately, the camera view angle for inspection is changed by rotating the wrist. Hence, it is suitable for the predominant wrist reactionless motion to perform this kind of inspection task. This task would be expected to perform several times in almost all kind of missions, such as construction, maintenance, debris removal and so on. Hence, this task is a good candidate for execution under reactionless motion control to reduce work efficiency.

We consider the following three tasks in order to accomplish the camera inspection.

1. The reactionless constraint (three-DoF)

2. End-effector orientation control (three-DoF)
3. Stabilization of the wrist position

The third one is due to the following reason: a large deflection of the wrist might induce a collision problem and a deviation of camera view angle.

The above tasks are simultaneously realized through the theory of task priority [29]. In this theory, the tasks are assigned the priorities according to their relative importance. The highest priority task, which is called the *primary task*, can be accomplished without the effects from lower priority tasks. Hence, lower priority tasks must be designed not to disturb the higher priority tasks. In order to ensure the prioritization, lower priority tasks are projected to the null-space of all-higher priority tasks. We will make a control command according to this theory.

4.2.1 Control command

We regard the reactionless constraint as the primary task, the end-effector orientation control is the second one and the wrist position stabilization is the third one. Then, the control command of the joint velocity considering the above priorities can be obtained as follows:

$$\dot{\boldsymbol{\theta}}^{ref} = \bar{\mathbf{J}}_{\omega_e}^+ \boldsymbol{\omega}_e^{ref} + k_g \mathbf{P} \mathbf{J}_{v_w}^T \Delta \mathbf{p}_w \quad (4.5)$$

where, $\boldsymbol{\omega}_e \in \mathbb{R}^3$ is angular velocity of the end-effector, $\bar{\mathbf{J}}_{\omega_e} = [\mathbf{J}_{\omega_e} \mathbf{P}_{RNS}] \in \mathbb{R}^{3 \times 7}$ is the restricted Jacobian matrix, \mathbf{J}_{ω_e} and $\mathbf{J}_{v_w} \in \mathbb{R}^{3 \times 7}$ stand for the Jacobian with respect to angular velocity of the end-effector and wrist linear velocity. $\mathbf{P} = \mathbf{P}_{RNS}(\mathbf{E} - \bar{\mathbf{J}}_{\omega_e}^+ \bar{\mathbf{J}}_{\omega_e})$ projects an arbitrary vector onto the null-space of the primary and second tasks [30]. $\Delta \mathbf{p}_w (= \mathbf{p}_w - \mathbf{p}_w^{init}) \in \mathbb{R}^3$ is wrist-position deflection from the initial one, k_g is a gradient gain.

The structure of the control command is as follows. The first term is the end-effector orientation control projected onto the null-space of the coupling

inertia matrix; this term can accomplish the end-effector orientation control ensuring the reactionless constraint. The second term minimizes the following potential function to stabilize the wrist position:

$$V = \frac{1}{2} \|\Delta \mathbf{p}_w\|^2. \quad (4.6)$$

This term does not disturb the higher priority tasks because it is projected onto the null-space of all higher priority tasks.

Here, it must be noted that $\bar{\mathbf{J}}_{\omega_e}^+$ includes the algorithmic singularities, which occur when the end-effector control and the reactionless constraint are conflict. The details of this singularity will be described below.

4.2.2 Numerical simulation

In what follows, we examine the performance under (4.5) by comparing to the following conventional inverse Jacobian controller with motionless of the positioning subchain:

$$\dot{\boldsymbol{\theta}}_W^{ref} = \mathbf{J}_{W\omega_e}^{-1} \boldsymbol{\omega}_e^{ref} \quad (4.7)$$

$$\dot{\boldsymbol{\theta}}_P^{ref} = \mathbf{0} \quad (4.8)$$

We assume following two situations: (i) observation of a satellite to be serviced (Fig. 4.3 (a)) and (ii) inspection for own satellite mounted devices (Fig. 4.3 (b)). First, we verify the satellite observation case. The initial configuration is set as $[-90 \ -30 \ 0 \ -70 \ 180 \ -30 \ 0]^T$ deg as shown in Fig. 4.3 (a), the reference angular velocity is $\boldsymbol{\omega}_e^{ref} = \pi[s(t) \ 0 \ 0]^T$, where $0 \leq s(t) \leq 1$ denotes a fifth-order polynomial interpolation. The simulation was conducted with the simulation time 20 s. The simulation results are displayed in Fig. 4.4. These were obtained with $k_g = 100$. In both methods, it can be seen that the end-effector task is accomplished. It is also seen that the base attitude deviation is not observed under reactionless motion control. The reactionless task can be realized with the relatively small motion of the

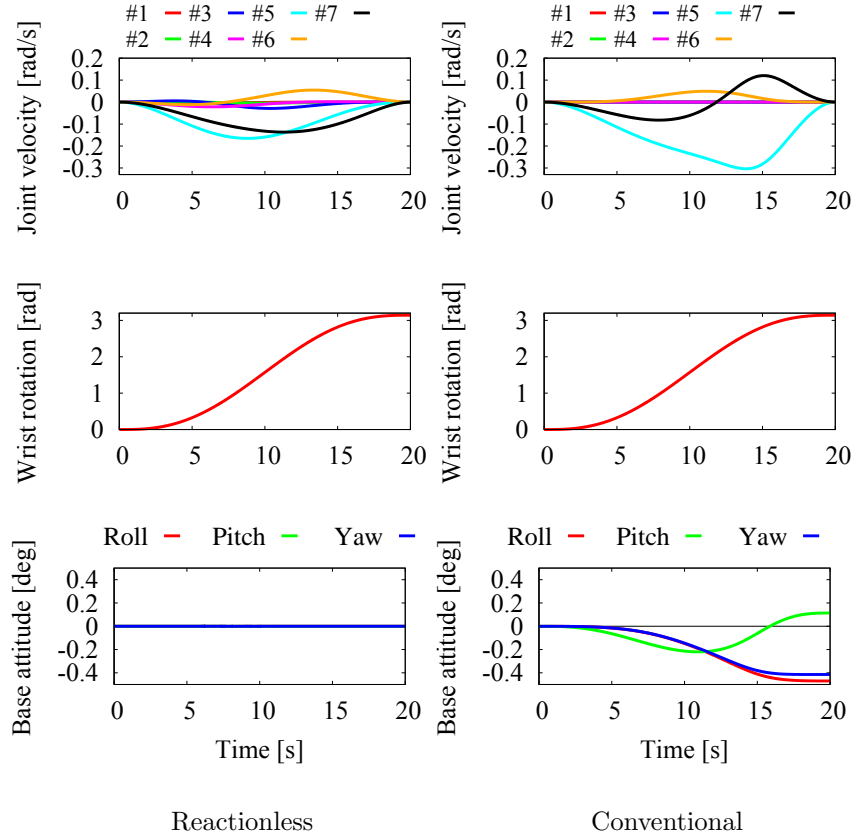


Fig. 4.4: Simulation result under the satellite observation mission (Fig. 4.3 (a)).

positioning subchain, see the figure of joint velocity. We should note that a relatively large base attitude deviation¹ was induced under the conventional control method, despite the small inertia parameters of the wrist.

In the second case, we assume that the initial configuration is set to $[90 \ -20 \ 180 \ 110 \ 0 \ 20 \ 0]^T$ deg as shown in Fig. 4.3 (b), the desired end-effector velocity is $\omega_e^{ref} = \pi[0 \ 0 \ -s(t)]^T$ rad/s. The other conditions are the same as the previous ones. The simulation result is displayed in Fig. 4.5. First, it

¹The limitation of the base attitude deviation is 0.05 deg in the ETS-VII missions.

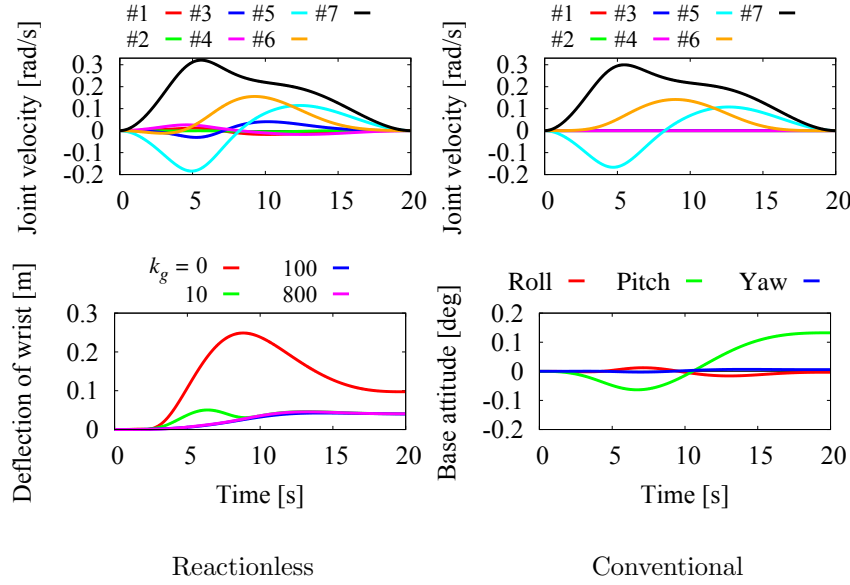


Fig. 4.5: Simulation result under the inspection of own-satellite mounted devices (Fig. 4.3 (b)).

becomes apparent that the effect of the third task leads to a sufficiently small deviation from the initial wrist position as shown in Fig. 4.5. In the case of the conventional controller, the relatively large base attitude deviation is also confirmed.

In summary, in the inspection task, even with the small mass and inertia moment of the wrist subchain, a large base attitude deviations were observed, while the reactionless motion task does not produce any base attitude deviation. From the results, we can conclude that reactionless motion control is suitable under the inspection task.

4.2.3 The algorithmic singularities within the reactionless inspection task

Problem statement

In this subsection, we deal with the singularities within the proposed reactionless task. Within the reactionless camera inspection, there are three types of singularity, as follows:

- Kinematic singularity: $\det(\mathbf{J}_{\omega_e} \mathbf{J}_{\omega_e}^T) = 0$
- Singularities of the coupling inertia matrix: $\det(\tilde{\mathbf{M}}_{\omega_m} \tilde{\mathbf{M}}_{\omega_m}^T) = 0$
- Algorithmic singularities: $\det(\bar{\mathbf{J}}_{\omega_e} \bar{\mathbf{J}}_{\omega_e}^T) = 0$ with non-singular \mathbf{J}_{ω_e} and full row-rank $\tilde{\mathbf{M}}_{\omega_m}$

Among them, kinematic singularities have been much discussed by various researchers, e.g. [31, 32]. From these results, the kinematic singularity can be dealt with through some singularity treatment techniques. The most well-known one is the damped least-squares inverse (DLS) [33]. Using these method, growth up of the joint velocity can be suppressed through adding a damping factor. A drawback of this method is causing an error on the task space, both speed and direction. On the other hand, we have proposed an another method, which is referred to as the *Singularity Consistent method* [34]. With the method, the manipulator can follow the desired path without causing a large joint velocity ². In both method, the feasibility has been verified under the kinematic singularities. Hence, we will not pay attention to this type of singularity below.

On the other hand, the second and third one have not been treated well. However, the singularities of the coupling inertia matrix is not a problem on the inspection task, because we use the null-space of the coupling inertia

²The term “Path” is distinguished from “Trajectory”: the former one means geometrical path and the later one includes time-parameter.

matrix. In (4.5), the rank of $\bar{\mathbf{J}}_{\omega_e}$ depends on the condition of \mathbf{J}_{ω_e} only, since the rank of \mathbf{P}_{RNS} cannot be lower than 3 with any configurations: e.g. at the singular configuration the rank increases more than 4. Hence, we will not also pay attention to this type of singularities.

On the other hand, we have to deal with the algorithmic singularities. The inversion of $\bar{\mathbf{J}}_{\omega_e}$ can be rewritten through SVD in the following form:

$$\bar{\mathbf{J}}_{\omega_e}^+ = \frac{1}{\sigma_1} \mathbf{v}_1 \mathbf{u}_1^T + \frac{1}{\sigma_2} \mathbf{v}_2 \mathbf{u}_2^T + \frac{1}{\sigma_3} \mathbf{v}_3 \mathbf{u}_3^T \quad (4.9)$$

where $\sigma_1 \geq \sigma_2 \geq \sigma_3$ are the singular values, $\mathbf{v}_i \in \mathbb{R}^7$, $\mathbf{u}_i \in \mathbb{R}^3$ are the left and right singular vectors associated with σ_i . Near the singularities, the last term of (4.9) takes a large value due to a small value of σ_3 . Unfortunately, this type of singularity is too complicated to find out their distribution through analytic approach. In what follows, we show an example of the algorithmic singularity through numerical simulation. We assume the inspection task with the same initial configuration that was used in the satellite observation task as shown in Fig. 4.3 (a). On the other hand, the desired angular velocity was commanded as $\boldsymbol{\omega}_e^{ref} = [0 \ -0.2 \ 0]^T$ rad/s. The simulation results are displayed in Fig. 4.6. In the graphs, the solid line in black represents the time when the manipulator is passing through near the singularity ($t \approx 2.57$). At that time, the determinant of $\bar{\mathbf{J}}_{\omega_e}$ takes a small value without causing $\det(\mathbf{J}_{\omega_e} \mathbf{J}_{\omega_e}^T) = 0$ and $\det(\tilde{\mathbf{M}}_{\omega_m} \tilde{\mathbf{M}}_{\omega_m}^T) = 0$ as shown in Fig. 4.6. Hence, this singularity can be recognized as the algorithmic one. Within the near singularity, we observe that joint 5 and 7 rotate around opposite direction with large joint velocity. This kind of behavior has been observed at the singularity of Euler angle [35] and the kinematic singularity of wrist assemblies. From the empirically obtained results, we should emphasize that this algorithmic type of singularity does not seem to happen frequently.

In what follows, we will verify two singularity techniques on this singularity.

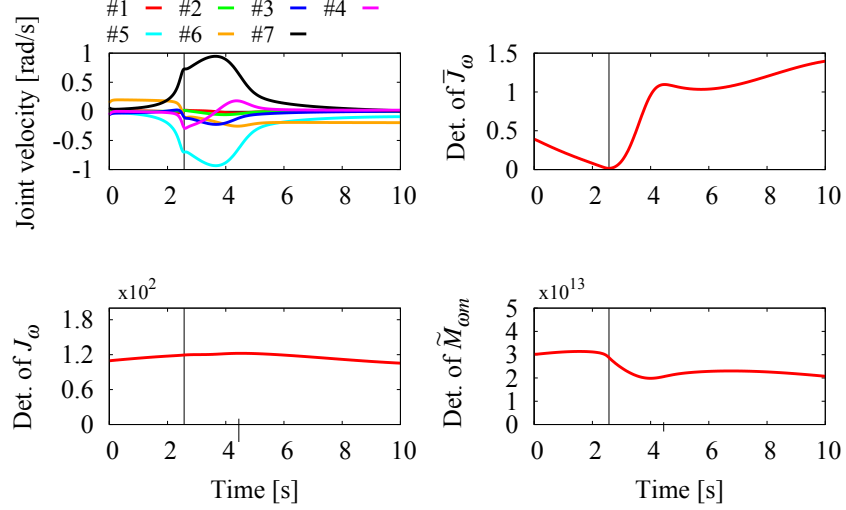


Fig. 4.6: An example of the algorithmic singularity within the proposed method.

The damped least-squares inverse based singularity treatment

The damped least-squares inverse is a well-known approach for singularity problems. Under the method, a damping factor is inserted into the denominators in (4.9) to avoid causing a large joint velocity. However, instead of the stable joint motion, a task space tracking error has to be caused. Among various types of the damped least-squares inverse, the damped least-squares inverse with numerical filtering does not induce a large error. Hence, we make use of this method in this work.

By using this method, the inverse matrix of $\bar{\mathbf{J}}_{\omega_e}$ is obtained as:

$$\bar{\mathbf{J}}_{\omega_e}^\# = \bar{\mathbf{J}}_{\omega_e}^T \left(\bar{\mathbf{J}}_{\omega_e} \bar{\mathbf{J}}_{\omega_e}^T + \lambda^2 \mathbf{u}_3 \mathbf{u}_3^T \right)^{-1} \quad (4.10)$$

where λ is a damping factor, $\mathbf{u}_3 \in \mathbb{R}^3$ is the left singular vector associated with the minimum singular value σ_3 , $(\cdot)^\#$ represents the damped least-squares inverse. Replacing the pseudoinverse solution with the damped least one, we

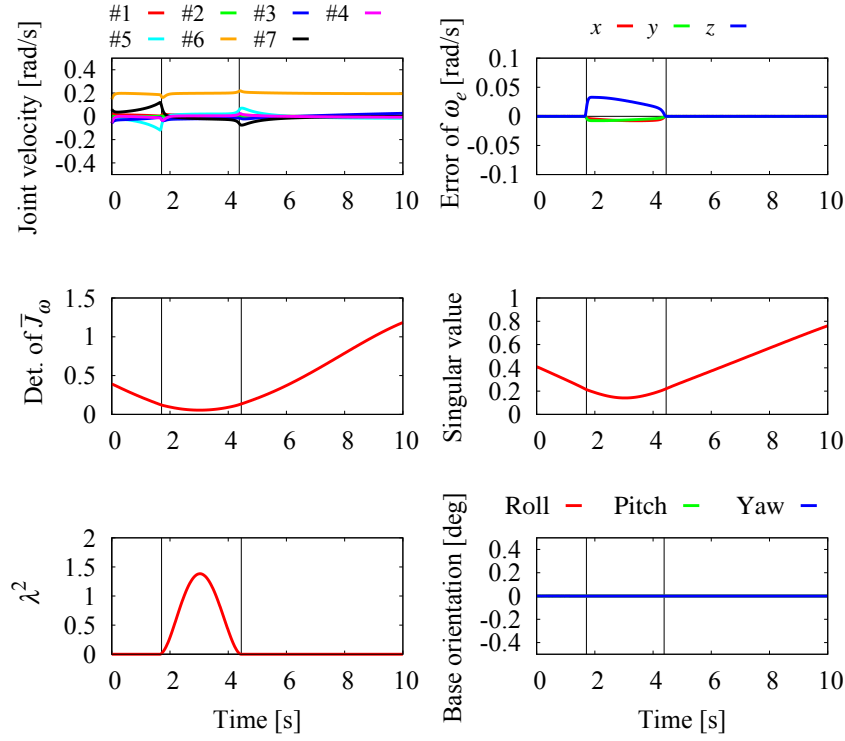


Fig. 4.7: Simulation results under the damped least-squares inverse with numerical filtering.

can deal with the singularity problem.

Through Singular Value Decomposition, (4.10) can be rewritten as:

$$\bar{J}_{\omega_e}^\# = \sum_{i=1}^2 \frac{1}{\sigma_i} \mathbf{v}_i \mathbf{u}_i^T + \frac{\sigma_3}{\sigma_3^2 + \lambda^2} \mathbf{v}_3 \mathbf{u}_3^T \quad (4.11)$$

Comparing it with (4.9), we can confirm that the damped least square inverse with numerical filtering inserts the damping factor into only the last term that is related to the minimum singular value.

Based on [33], the damping factor is obtained as follows:

$$\lambda^2 = \begin{cases} 0 & \varepsilon < \sigma_3 \\ (1 - \frac{2\sigma_3^2}{\varepsilon^2} + \frac{\sigma_3^4}{\varepsilon^4})\lambda_{max}^2 & \sigma_3 \leq \varepsilon \end{cases} \quad (4.12)$$

where ε defines the singular region, which has been conveniently introduced in the neighborhood of the singularity, λ_{max} sets the maximum value of the damping factor. Note that we added an additional term, which is the σ_3^4 related term, into (4.12) to obtain a smooth transition on the border of the singular region, because the original one did not consider the continuity at the first differential in terms of σ_3 .

The performance of the damped least-squares inverse for the algorithmic singularity is verified via numerical simulation. The simulation conditions are the same as in Section 4.2.3. The singular region is defined as $\varepsilon = 0.2$ and the maximum damping value set to $\lambda_{max}^2 = 2$.

The results are displayed in Fig. 4.7. In the graphs, the singular region is indicated as the time duration between the two black lines ($1.71 \text{ s} \leq t \leq 4.18 \text{ s}$). From the results, the growth up of the joint velocity can be avoided through the damping factor. However, the end-effector tracking error can be observed within the singular region. This is caused by adding the damping factor into the last term in (4.11). On the other hand, the base attitude deviation is not induced even if within the singular region.

The singularity consistent method with a constant scalar

From the result of DLS method, it was confirmed that the task space error happened. On the other hand, as mentioned already, we have proposed a different type of singularity treatment technique; the method has been referred to as the Singularity Consistent method. While the DLS method does not use the singular direction, which is the motion of \mathbf{u}_3 , the singularity consistent method actively makes use of the motion direction. The feature of this method is that a manipulator can follow the direction of the desired

end-effector velocity, correctly. An error only appears at the speed. If we consider a tele-operated task, the speed error is not a problem because that kind of task does not need to follow the desired trajectory.

Among various types of singularity consistent method, we make use of a natural motion type of that. Natural motion is a motion whose end-effector velocity is proportional to the determinant of the corresponding matrix. This method does not need to define the singular region and to switch the control input on its boundary.

Using this method, we can obtained the inversion of $\bar{\mathbf{J}}_{\omega_e}$ as follows:

$$\bar{\mathbf{J}}_{\omega_e}^+ = b \sum_{i=1}^3 \mu_i \mathbf{v}_i \mathbf{u}_i^T \quad (4.13)$$

$$\mu_i = \prod_{j=1, j \neq i}^3 \sigma_j \quad (4.14)$$

where b is a constant scalar. In (4.14), we can see that μ_1 and μ_2 become small near the singularity, because these are proportional to the minimum singular value that becomes 0 at the singularity. Hence, the \mathbf{v}_3 related term is actively used on this method.

We verify the performance of this method through numerical simulation. The simulation conditions are the same as the DLS case. Empirically, the constant scalar was set to $b = 1.7$. In addition, to avoid a large joint velocity obtained from the null-space term, we multiply the term by the determinant of $\bar{\mathbf{J}}_{\omega_e}$.

The simulation results are displayed in Fig. 4.8. The results show that the rapid change of the joint velocity can be avoided. In addition to this feature, the end-effector was followed the desired velocity direction y . Under tere-operated tasks, the determination of b was discussed in [36].

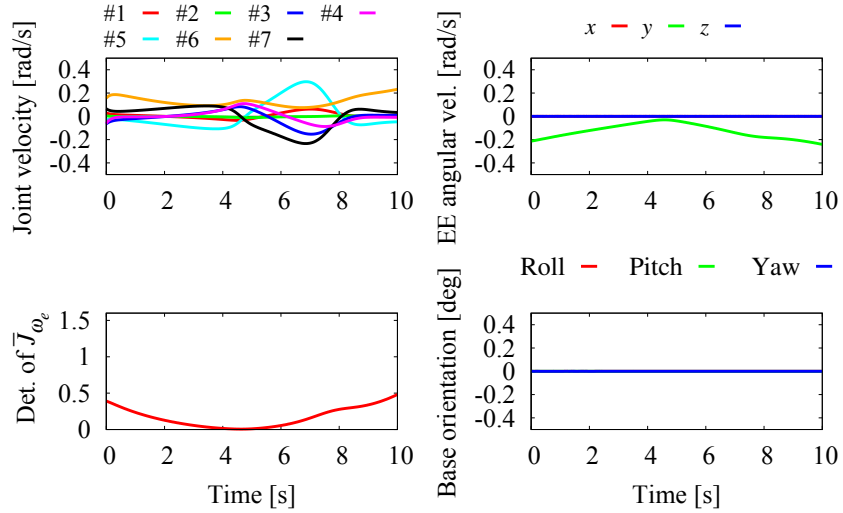


Fig. 4.8: Simulation results under the singularity consistent method.

4.3 Point-to-point positioning task

As the second reactionless task, we focus on point-to-point (PTP) positioning tasks of the end-effector. PTP positioning tasks would be used several situation such as pre-positioning task of the camera inspection, assembly and so on. Among the several positioning tasks, we restrict our attention to a specific subset of PTP tasks: arm reconfiguration tasks wherein the hand does not hold an object. It would be desirable to execute such tasks under reactionless motion control.

However, this is impossible for arbitrary points since reactionless motions are quite restricted. Nevertheless, reactionless motion can be useful if the PTP motion is planned appropriately. One possibility is to combine two reactionless motions with a non-restricted PTP motion that induces the base disturbance. This method was originally proposed in [20]; it has been referred to as the *3-Phase method* and applied to a planar flexible base robots. Note that despite the advantage of the method was verified with a planar flexible

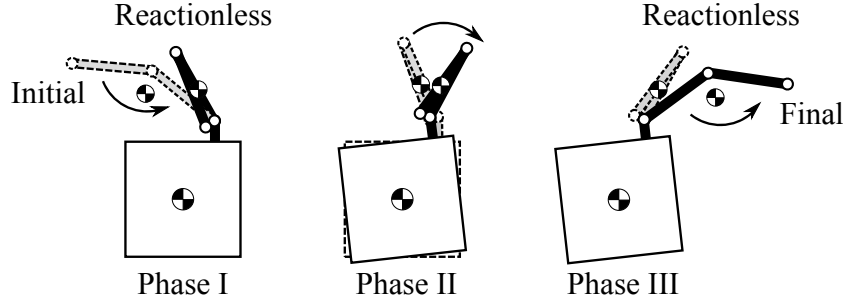


Fig. 4.9: A motion obtained via the 3-Phase method.

base robots, the cases of free-floating base robots and also three-dimensional models have not been discussed before. We verify the performance of this method with the three-dimensional free-floating robot.

4.3.1 The 3-Phase method

First, we review the 3-Phase method. The 3-Phase method deals with the following issue: find a joint path that connects specific initial and final configurations with three sub-paths. We divide a motion into three Phase, which are Phase I, II and III, according to the three sub-paths. In Phase I and III, reactionless motion is used. In Phase II, these two reactionless motion paths are connected via a joint path that is not reactionless. The primary concern is how to determine the three sub-paths to obtain small base disturbance during the PTP sub-paths in Phase II. In [20], a folded arm configuration as shown in Fig. 4.9 was employed in Phase II. Using this configuration, the base disturbance can be reduced. We provide a theoretical argument of reaction reduction with the folded configuration in what follows. The coupling angular momentum, which is the base reaction with dimension of momentum,

can be represented in the following form:

$$\begin{aligned} \tilde{M}_{\omega m} \dot{\boldsymbol{\theta}} = & \left\{ \sum_{i=1}^n \mathbf{I}_i \mathbf{J}_{\omega_i} \right\} \dot{\boldsymbol{\theta}} + \\ & \left\{ \sum_{i=1}^n m_i [\mathbf{r}_i^{\times}] \mathbf{J}_{v_i} \right\} \dot{\boldsymbol{\theta}} - \left\{ m_{com} [\mathbf{r}_{com}^{\times}] \mathbf{J}_{com} \right\} \dot{\boldsymbol{\theta}}, \end{aligned} \quad (4.15)$$

It is apparent that the coupling angular momentum consists of three kinds of angular momentum. The first term represents the angular momentum induced by purely rotational motion of each link; the second and third term are the angular momentum arising from the moment of the linear momentum of each link and the CoM of the manipulator. The coefficient matrix of the first term is related to the inertia tensor of the manipulator. Hence, at the folded configuration, this term becomes the smallest value. On the other hand, the second and third term are related to the CoM positions. The base reaction related to these term also takes small amount using the folded configuration, because the distance along which the manipulator CoM moves becomes short, as shown in Fig. 4.9. In addition, the norm of \mathbf{r}_i and \mathbf{r}_{com} become small value at the configuration. Hence, the angular momentum related to the linear momentum of each link can be reduced. For this reason, the folded configuration is used in Phase II.

4.3.2 Verification via numerical simulations

We verify the performance of the 3-Phase method via numerical simulations, compared with several conventional controllers. The initial configuration is $[-20 \ -40 \ 0 \ -60 \ 180 \ 180 \ 0]^T$ deg; the final one is $[-120 \ 50 \ 0 \ -60 \ 180 \ 180 \ 0]^T$ deg. Note that these two configurations cannot be linked via reactionless motion. The motion in Phase I is obtained from the initial configuration toward a folded configuration (FA-1). Phase III is determined as a reversed (reactionless) motion starting from the final configuration toward other folded configuration (FA-2). These two reactionless motions are

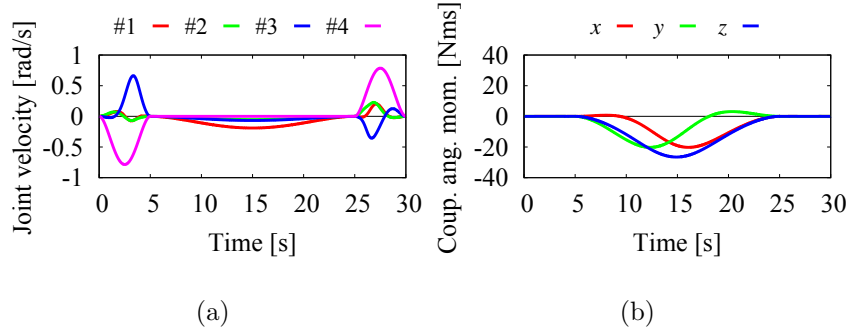


Fig. 4.10: The simulation results under the 3-phase method: (a) the joint velocity and (b) the coupling angular momentum.

obtained as the second term in (4.2) as follows:

$$\dot{\theta}^{ref} = \frac{\dot{\theta}_4^{ref}(t)}{n_4} \begin{bmatrix} \mathbf{n} \\ 0 \end{bmatrix} \quad (4.16)$$

$$\dot{\theta}_4^{ref}(t) = \dot{\theta}_4^{des}(t) + k\Delta\theta_4(t) \quad (4.17)$$

where n_4 is the fourth element of \mathbf{n} , $\theta_4(t)^{des}$ is the desired trajectory of joint 4; $\Delta\theta_4(t) = \theta_4^{des}(t) - \theta_4$ is the tracking error. k is a feedback gain. The two folded configurations are distinct and uniquely defined as resultant configurations along the respective reactionless motion, wherein $\theta_4 = -\pi$ rad. In Phase I and III, the motions were executed in 5 s, and Phase II in 20 s.

For the comparison, the same positioning task was executed under the joint space interpolation with straight line (JS-C), the inverse Jacobian controller (IJ-C) and the transposed Jacobian controller (TJ-C). For the task space controllers (IJ and TJ-C), the final condition was set to the final position of the end-effector in the 3-Phase method as $[-1.7 \ 0.45 \ 1.7]^T$ m. The three controllers were executed in 30 s. Note that orientation of the end-effector is not considered for the sake of simplicity. Hence, only the positioning subchain was driven.

First, we show the results obtained in the 3-Phase method in Fig. 4.10.

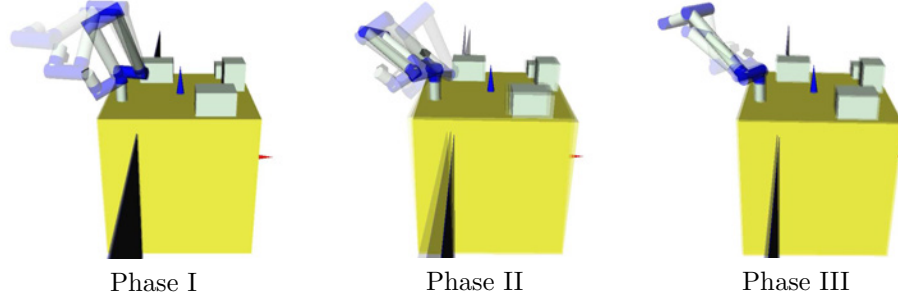


Fig. 4.11: The snapshot of the motion obtained via the 3-phase method.

Table 4.2: The maximum value of the base deviation.

	Maximum deviation [deg]	Ratio
3-Phase	1.95	1.00
JS-C	3.61	1.84
IJ-C	3.21	1.64
TJ-C	3.85	1.96

From the results, the joint motion can be smoothly obtained and only Phase II introduced the coupling angular momentum.

To evaluate the performance in terms of the base reaction, we compare the base attitude deviations under all methods. The time profiles of the base attitude deviation are displayed in Tab. 4.2. The maximum deviation and the its ratio between the compared methods and the 3-phase are shown in Tab. 4.2.

From the results, it can be seen that the maximum deviation under the 3-phase method is about two times smaller than that under the others. Hence, we can conclude that the 3-phase method has a advantage in terms of the base reaction.

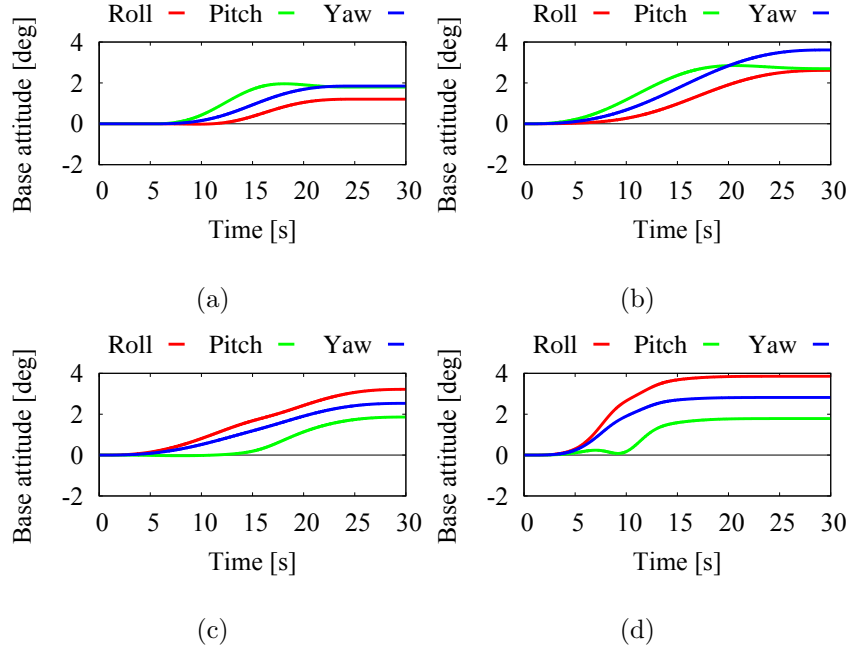


Fig. 4.12: The base attitude deviations under the all methods: (a) 3-phase method, (b) JS-C, (c) IJ-C and (d) TJ-C.

4.4 Deployment task

Finally, we discuss the possibility of reactionless motion control under the deployment motion task from a stowed configurations. When launching a free-floating space robot into orbit, the manipulator has to be stowed to overcome several loads. These configurations are referred to as the *stowed configurations*. An example is displayed in Fig. 4.13 (upper left). During on-orbit experiments, deployment from the configuration has to be executed at least few times. We propose reactionless motion control in the following two case: (i) full reactionless deployment and (ii) partial reactionless deployment.

4.4.1 Full reactionless task

First, we examine the possibility of a deployment task under fully reactionless condition. For the sake of simplicity, we only use the positioning subchain because the effect of wrist motion is relatively small at this motion task. As a result, the DoF of reactionless motion becomes one due to considering only the positioning subchain. Therefore, the reactionless motion path is uniquely determined according to a initial configuration. The final (deployed) configuration can be selected as any configurations along the reactionless path. The selection will depend upon the subsequent task. The benefit is that the speed/acceleration along the reactionless path connecting the two configurations can be set freely that allows for a very time-efficient deployment.

We define the candidates for the stowed configuration of the our manipulator model as follows:

$$\begin{aligned} \boldsymbol{\theta}_{st} = \{ \boldsymbol{\theta} \in \mathbb{R}^7 | \theta_i = \pm\pi/2, \theta_j = 0, \pm\pi, \forall \theta_k \} \\ (i = 1, 2, j = 3 \text{ to } 5, k = 6, 7) \end{aligned} \quad (4.18)$$

Among them, we pick up a configuration that is well-conditioned for the reactionless motion: $[\pi/2 \ -\pi/2 \ 0 \ -\pi \ \pi \ \pi \ 0]^T$ rad. Snapshots of the deployment sequence during 30 s are shown in Fig. 4.13. The motion was obtained via (4.17) with the constant speed of joint 4: $\dot{\theta}_4^{des} = 0.183$ rad/s. It can be seen that the reactionless path is passing through an appropriate point for an inspection task at $t = 30$ s. In that case, this motion task can be useful. The possibility of the reactionless deployment was confirmed at least this case.

However, it should be noted that this motion task is only available when a useful reactionless motion path can be prepared for specific tasks. Instead of the full-reactionless motion, we propose a deployment method using reactionless motion partially based on the 3-phase method in what follows.

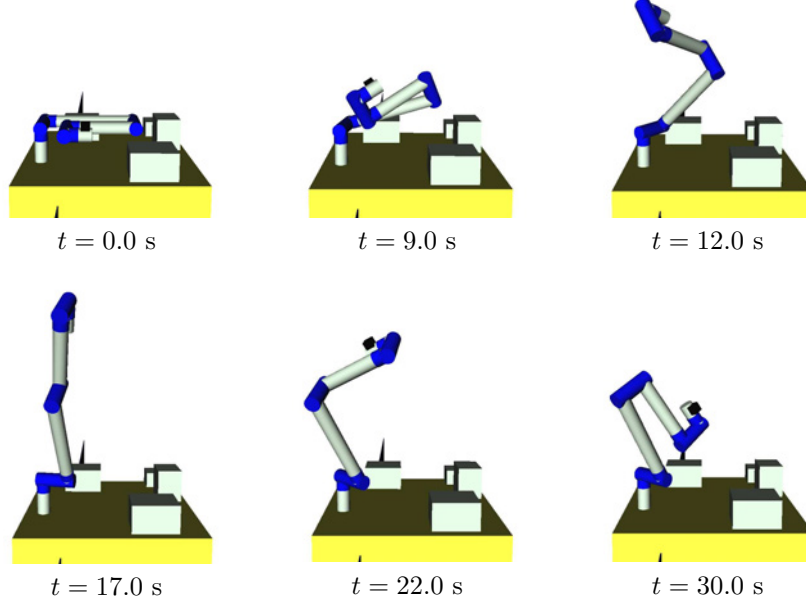


Fig. 4.13: Motion snapshots from the deployment task under reactionless motion control.

Partial reactionless deployment

Here, we present a deployment motion task for reduction of the base reaction. We use a specific part of the 3-phase method; in particular Phase II and III. Because the stowed configuration is a folded configuration, the sub-part of the 3-phase method can be used, straightforwardly. From the results of the 3-phase method, the base reaction can be reduced.

We show an example of the motion task. The pre-positioning task for an inspection task, which was shown in Fig. 4.3 (b), is assumed. The initial configuration is set to the same stowed configuration that was used before. The final configuration is set to $[90 \ 50 \ 0 \ -300 \ 0 \ 20 \ 0]^T$ deg. The middle point configuration at which the two motions are switched is obtained as the terminal configuration from the final one to the elbow folded configuration

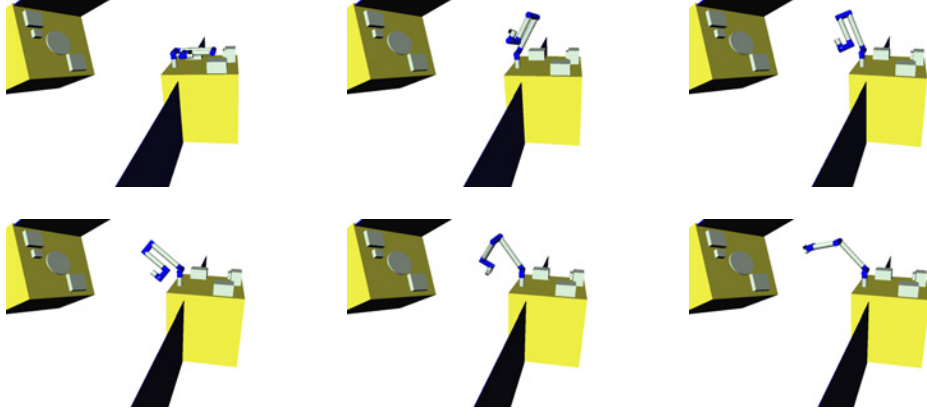


Fig. 4.14: The snapshot of the motion under partial reactionless deployment.

$\theta_4 = \pi$ rad.

The snapshot of the motion task is displayed in Fig. 4.14. For comparison, the joint space controller with straight line trajectory was performed under the same condition. The snapshot is displayed in Fig. 4.15. From the results, the maximum base attitude deviation under partial reactionless task was 5.48 deg; on the other hand, 7.66 deg base attitude was observed under the comparison controller. Hence, 28.5% reduction of the base attitude deviation can be realized.

4.5 Summary

In this chapter, we discussed the motion tasks that are suitable for execution under reactionless motion control. The following three tasks were considered: (i) inspection task using a hand camera, (ii) PTP positioning task and (iii) deployment task from the stowed configuration. We showed that the proposed methods using reactionless motion control has a advantages compared with several conventional controllers in terms of the base reaction.

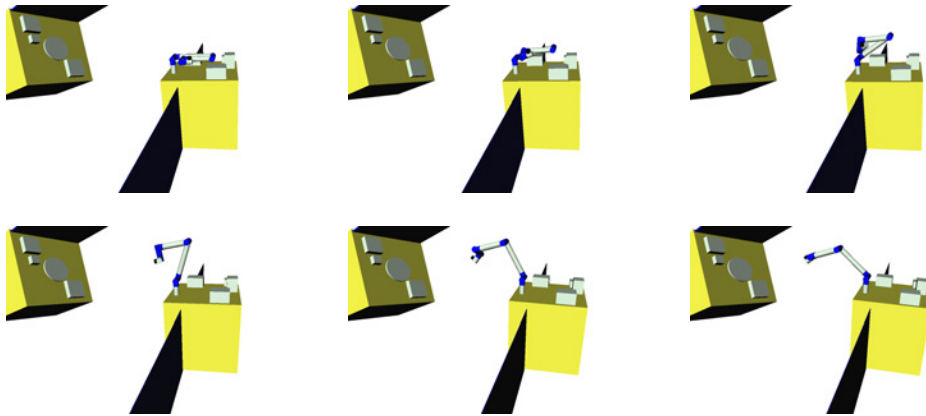


Fig. 4.15: The snapshot of the motion under the conventional joint space interpolation.

Chapter 5

Energy Consumption Analysis

So far, reaction wheels have been used to stabilize the base attitude against the base reaction induced by a manipulator motion. However, as explained in Chapter 1, the output torque of reaction wheels are far smaller than the base reaction. In addition to this problem, it is known that reaction wheels need a large amount of energy if a large output torque is produced [24]. On the other hand, reactionless motion control need not use reaction wheels. Hence, we can expect that energy consumption during a task can be reduced through reactionless motion control. In fact, we will show that reactionless motion coincides with the instantaneous minimum energy motion.

5.1 Kinetic energy

In this work, we assume that kinetic energy is used to evaluate the energy consumption. For the sake of simplicity, we ignore the energy losses arising from friction, heat and electric part. The kinetic energy of free-flying space robots can be written as [4, 18]:

$$T = \frac{1}{2} \boldsymbol{\omega}_b^T \tilde{\mathbf{M}}_{\omega} \boldsymbol{\omega}_b + \boldsymbol{\omega}_b^T \begin{bmatrix} \tilde{\mathbf{M}}_{\omega m} & \tilde{\mathbf{M}}_{\omega r} \end{bmatrix} \begin{bmatrix} \dot{\boldsymbol{\theta}} \\ \dot{\boldsymbol{\phi}} \end{bmatrix} + \frac{1}{2} \begin{bmatrix} \dot{\boldsymbol{\theta}}^T & \dot{\boldsymbol{\phi}}^T \end{bmatrix} \begin{bmatrix} \tilde{\mathbf{M}}_m & \mathbf{0} \\ \mathbf{0} & \tilde{\mathbf{M}}_r \end{bmatrix} \begin{bmatrix} \dot{\boldsymbol{\theta}} \\ \dot{\boldsymbol{\phi}} \end{bmatrix} \quad (5.1)$$

where, the first term on the r.h.s. represents the partial kinetic energy stemming from base rotation, the second term is the coupling kinetic energy between the base and the manipulator or the reaction wheels. Finally, the third term is the partial kinetic energy produced by actuators.

With the assumption $\omega_b \approx \mathbf{0}$, (5.1) can be simplified as follows:

$$T = \frac{1}{2} \dot{\boldsymbol{\theta}}^T \tilde{\mathbf{M}}_m \dot{\boldsymbol{\theta}} + \frac{1}{2} \dot{\boldsymbol{\phi}}^T \tilde{\mathbf{M}}_r \dot{\boldsymbol{\phi}} \quad (5.2)$$

In addition, from angular momentum conservation, the reaction wheel speed can be represented as a function of joint velocity, $\dot{\boldsymbol{\phi}} = -\tilde{\mathbf{M}}_{\omega r}^{-1} \tilde{\mathbf{M}}_{\omega m} \dot{\boldsymbol{\theta}}$. Substituting the above equation into (5.2), we can obtain the kinetic energy as a function of the joint velocity as follows:

$$\begin{aligned} T &= \frac{1}{2} \dot{\boldsymbol{\theta}}^T \left(\tilde{\mathbf{M}}_m + \tilde{\mathbf{M}}_{\omega m}^T (\tilde{\mathbf{M}}_{\omega r} \tilde{\mathbf{M}}_r^{-1} \tilde{\mathbf{M}}_{\omega r}^T)^{-1} \tilde{\mathbf{M}}_{\omega m} \right) \dot{\boldsymbol{\theta}} \\ &= \frac{1}{2} \dot{\boldsymbol{\theta}}^T \left(\tilde{\mathbf{M}}_m + I_r^{-1} \tilde{\mathbf{M}}_{\omega m}^T \tilde{\mathbf{M}}_{\omega m} \right) \dot{\boldsymbol{\theta}} \\ &= \frac{1}{2} \dot{\boldsymbol{\theta}}^T \boldsymbol{\Lambda} \dot{\boldsymbol{\theta}} \end{aligned} \quad (5.3)$$

where, $\boldsymbol{\Lambda} = \boldsymbol{\Lambda}_m + \boldsymbol{\Lambda}_r$ is the inertia matrix of the manipulator under zero attitude deviation, $\boldsymbol{\Lambda}_m = \tilde{\mathbf{M}}_m$, $\boldsymbol{\Lambda}_r = I_r^{-1} \tilde{\mathbf{M}}_{\omega m}^T \tilde{\mathbf{M}}_{\omega m} \in \mathbb{R}^{n \times n}$ are that associated with the manipulator and the reaction wheels, respectively. In the above derivation, we assume that $\tilde{\mathbf{M}}_{\omega r} \approx \tilde{\mathbf{M}}_r$ and $\tilde{\mathbf{M}}_r = \text{diag}(I_r, I_r, I_r)$. Besides, we assume that the reaction wheels are arranged on each orthogonal axis of the base coordinate according to zero-momentum stabilization, and these inertia moments are same values.

5.2 Instantaneous minimum energy motion

Equation (5.3) represents the kinetic energy under zero base-attitude deviation. Using the same way as the coupling map [10], we can obtain the instantaneous minimum energy motion through SVD of the inertia matrix

$\Lambda = \Lambda_m + \Lambda_r$:

$$\Lambda = \sigma_1 \mathbf{u}_1 \mathbf{v}_1^T + \sigma_2 \mathbf{u}_2 \mathbf{v}_2^T + \cdots + \sigma_n \mathbf{u}_n \mathbf{v}_n^T \quad (5.4)$$

where σ_i ($\sigma_1 \geq \sigma_2 \geq \cdots \geq \sigma_n > 0$) is singular value, \mathbf{u}_i and \mathbf{v}_i are the left and the right singular vectors. In this equation, physically, \mathbf{v}_i stands for the normalized joint velocity and σ_i represents the kinetic energy produced by the joint motion \mathbf{v}_i . Because σ_n represents the instantaneous minimum kinetic energy, \mathbf{v}_n^T represents the instantaneous minimum energy motion.

5.3 Motion equivalence

Here, we compare reactionless motion and the instantaneous minimum energy motion via numerical analysis. For the sake of simplicity, we focus on models that have one-DoF reactionless motion, only.

5.3.1 Two-DoF planar manipulator

First, a two-DoF planar model is considered, which is shown in Fig. 3.1. The link lengths, masses and inertia moments are set to $l_i = 1.0$ m, $m_i = 100$ kg and $I_i = 8.3$ kgm² ($i = 1, 2$), respectively. The reaction wheel's mass and inertia moment are set to $m_r = 10$ kg, $I_r = 0.11$ kgm², respectively. The manipulator attachment position is defined as $r = 0.945$ m, $\psi = 0$ rad, whose meaning are same as Fig. 3.1.

Here, we consider the following cost function to evaluate the equivalence between reactionless motion and the instantaneous minimum energy motion:

$$C_{ratio} = \frac{T_{RNS}}{T_{min}} \quad (5.5)$$

where T_{RNS} , T_{min} are the kinetic energy under reactionless motion control and the instantaneous minimum one. Because $T_{RNS} \geq T_{min}$ at all configurations, $C_{ratio} \geq 1$ is ensured. C_{ratio} takes close to 1 means these motion are

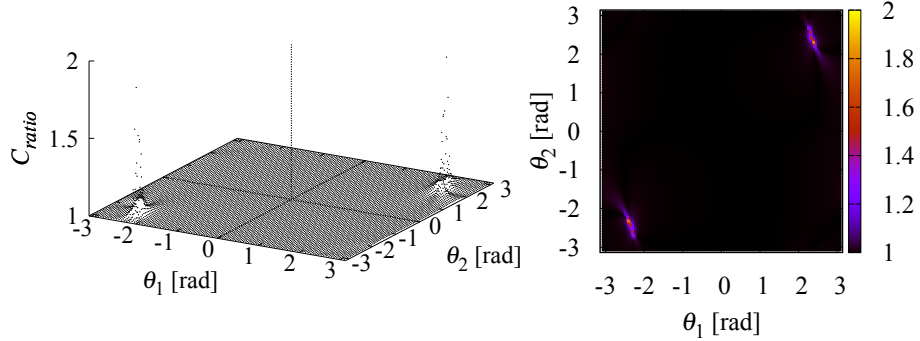


Fig. 5.1: The distribution of the cost function with the two-DoF model.

equivalent. This function will be calculated at 10000 points in the joint space with $-\pi \leq \theta_i \leq \pi$, ($i = 1, 2$). For each coordinate, joint angle are discretized with $\Delta\theta_i = 6.28 \times 10^{-2}$ rad. According to (5.4), $\dot{\theta}_{min}$ can be obtained as \mathbf{v}_2 and reactionless motion is obtained through SVD of the coupling inertia matrix.

The distribution of C_{ratio} is displayed in Fig. 5.1. From the result, we can confirm that $C_{ratio} \approx 1$ at almost all points. Indeed, the average of C_{ratio} is 1.002 among all points. Hence, these motions are highly equivalent in this model. Here, we should note that there are large errors in specific points. This non-correspondence is related to the singularity of the coupling inertia matrix.

5.3.2 Influence arising from parameters variation

Before discussing a spatial model, we should identify the influence arising from parameter variation. Here, we focus on total link mass and the CoM position of each link according to the following equation:

$$m_i^* = \alpha m_i \quad (5.6)$$

$$l_{ci}^* = \beta l_{ci} \quad (5.7)$$

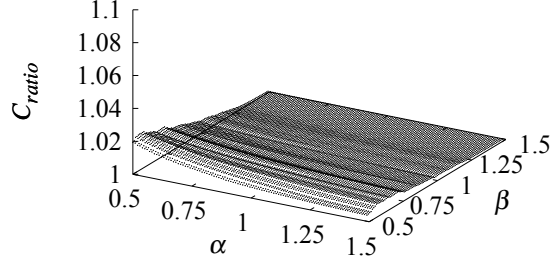


Fig. 5.2: This figure shows how the average of C_{ratio} is affected by parameter variation.

where $0.5 \leq \alpha \leq 1.5$, $0.5 \leq \beta \leq 1.5$ are scaling factors, m_i , $l_{ci} = l_i/2$ are the original mass and length between the each link CoM and each joint ($m_i = 100$ kg, $l_i = 1$ m). $(\circ)^*$ denotes the modified parameter.

Average of C_{ratio} under the parameter variation is displayed in Fig. 5.2. This figure shows that reactionless motion coincides with instantaneous minimum motion even if parameters are changed. In particular, high equivalence can be observed when α takes large values.

5.3.3 Four-DoF spatial manipulator

Here, we identify the equivalence with a four-DoF spatial manipulator. As the our manipulator model, the positioning subchain of the seven-DoF redundant manipulator is considered. The reaction wheel parameters are same as one which was used in the planar case. In this case, the same cost function

is also used to evaluate the equivalence. The calculation range is as follows:

$$\begin{aligned} -\pi &\leq \theta_i \leq \pi \\ \Delta\theta_i &= 0.125 \text{ rad } (i = 1, 3, 4) \end{aligned} \tag{5.8}$$

$$\begin{aligned} -\frac{\pi}{2} &\leq \theta_2 \leq \frac{\pi}{2} \\ \Delta\theta_2 &= 0.0628 \text{ rad} \end{aligned} \tag{5.9}$$

where, we restrict the range of joint 2 because almost all configurations over the above range have no meaning due to the collision with the satellite. Totally, the cost function is calculated at 6.25×10^6 points.

Because of too many parameters to draw graph, we show the distribution of C_{ratio} parametrized for joint 1 and 2. First, we show a distribution map which does not include large errors in Fig. 5.3 (a). The map was obtained with parametrized for $(\theta_1, \theta_2) = (-3.05, 0.403)$ rad. Except few configurations, reactionless motion coincides the energy minimum motion as seen in the planar case. However, we observe inconsistency with specific configurations. An example is shown in Fig. 5.3 (b) with parametrized for $(\theta_1, \theta_2) = (-\pi, 0)$ rad. Despite these large errors, the average value of C_{ratio} is 1.14. Hence, reactionless motion produces almost minimum energy. In what follows, we discuss the reason of the equivalence and the inconsistency.

5.4 Discussion about the equivalence

Here, we discuss why these motions are equivalent. To answer the question, we should identify a property of kinetic energy produced by both manipulator and reaction wheels under zero base-attitude deviation. This property

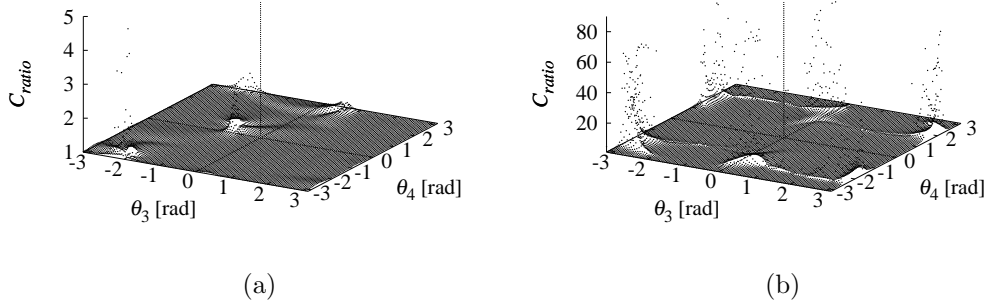


Fig. 5.3: The disutribution of cost function with the four-DoF spatial manipulator model: (a) regularly appearing distribution $(\theta_1, \theta_2) = (-3.05, 0.403)$ rad and (b) near the singularity $(\theta_1, \theta_2) = (-\pi, 0)$ rad.

appears in the inertia matrix. Λ_m and Λ_r are rewritten in the following form:

$$\Lambda_m = \sum_{i=1}^n \left\{ m_i \mathbf{J}_{vi}^T \mathbf{J}_{vi} + \mathbf{J}_{\omega i}^T \mathbf{I}_i \mathbf{J}_{\omega i} \right\} \quad (5.10)$$

$$\begin{aligned} \Lambda_r = \frac{1}{I_r} \sum_{i=1}^n \left\{ m_i^2 \mathbf{J}_{vi}^T \mathbf{r}_i^{\times T} \mathbf{r}_i^{\times} \mathbf{J}_{vi} + \mathbf{J}_{\omega i}^T \mathbf{I}_i \mathbf{I}_i \mathbf{J}_{\omega i} + \right. \\ \left. m_i \mathbf{J}_{\omega i}^T \mathbf{I}_i \mathbf{r}_i^{\times} \mathbf{J}_{vi} + [m_i \mathbf{J}_{\omega i}^T \mathbf{I}_i \mathbf{r}_i^{\times} \mathbf{J}_{vi}]^T \right\} \end{aligned} \quad (5.11)$$

where m_i , $\mathbf{I}_i \in \mathbb{R}^3$ are i th link mass and inertia tensor, \mathbf{J}_{vi} , $\mathbf{J}_{\omega i} \in \mathbb{R}^{3 \times n}$ stand for the Jacobian w.r.t. linear and angular velocity of each link, $\mathbf{r}_i \in \mathbb{R}^3$ is the position vector of i th link CoM w.r.t. the base CoM. Here, we assume general n -link manipulator model. Note that the base linear motion related terms are ignored for the sake of simplicity.

From (5.10), it can be seen that the kinetic energy induced by the manipulator motion is represented as a linear function in terms of the inertia parameters of manipulator. On the other hand, reaction wheel related energy is a quadratic function in terms of same parameters; it is also proportion to the inverse of the inertia moment of the reaction wheel, which is usually

enough smaller than 1. Hence, we can conclude that the reaction wheel producing kinetic energy is far larger than the manipulator's one. This feature would make reactionless motion potentially effective in terms of energy consumption because no usage of reaction wheels.

On the other hand, compared with the results in Fig. 3.2 (b) and Fig. 5.1, we can find that the inconsistency happens around the singularity of the coupling inertia matrix. In particular, at the singular configuration, any motion does not disturb the base attitude because the null-space of the coupling inertia matrix coincides with the tangential space of joint space $T_\theta(\mathbb{R}^2)$: namely an additional reactionless motion vector appears at the singularity. In this case, reactionless motion must be energy minimum. On the other hand, near the singularities, reactionless motion does not coincide with the instantaneous energy minimum motion, in general. Since the base disturbance is quite small near the singularity: e.g. reaction wheel is hardly needed, reactionless motion can be different from the minimum energy one.

5.5 Comparison study

5.5.1 Simulation condition

Finally, we evaluate the performance of using reactionless motion control in terms of energy consumption at the inspection maneuver. From the above analysis, reactionless motion is nearly energy minimum and reaction wheels are needed a large energy to compensate a base disturbance.

We consider the following cost functions to evaluate the performance:

$$C_{max} = \frac{1}{2} \max_{t_0 \leq t \leq t_f} \left(\dot{\boldsymbol{\theta}}^T(t) \boldsymbol{\Lambda} \dot{\boldsymbol{\theta}}(t) \right) \quad (5.12)$$

$$C_{sum} = \frac{1}{2} \int_{t_0}^{t_f} \dot{\boldsymbol{\theta}}^T(t) \boldsymbol{\Lambda} \dot{\boldsymbol{\theta}}(t) dt \quad (5.13)$$

In order to realize zero base-attitude deviation with reaction wheels, the

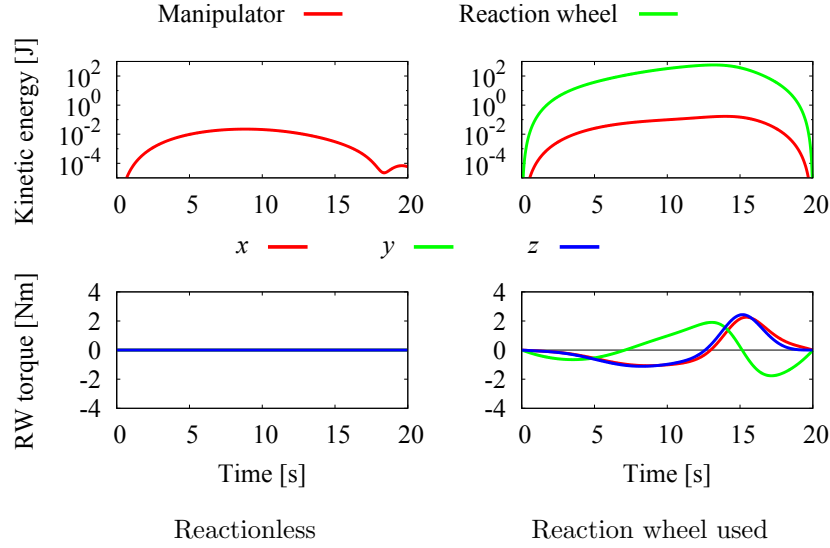


Fig. 5.4: An example of energy consumption comparison.

reaction wheel torque must ensure the following condition:

$$\boldsymbol{\tau}_r^{ref} = -\frac{d}{dt}(\tilde{\mathbf{M}}_{\omega m} \dot{\boldsymbol{\theta}}^{ref}(t)) \quad (5.14)$$

where $\dot{\boldsymbol{\theta}}^{ref}$ is the pre-defined reference control command for the manipulator.

We compare the above costs under the camera inspection task under five conditions with some initial configurations and the desired motions. At all of them, simulation time is set as 20 s and the comparison controller is the inverse Jacobian controller using only the wrist assembly as explained in the previous section.

5.5.2 Simulation results

First, we show an example. The conditions were same as ones which were considered in Chapter 4 (the case of Fig. 4.3 (a)). The results are displayed in Fig. 5.4. We can see that the kinetic energy produced by the reaction wheel is quite larger than that by the manipulator motion. As a result,

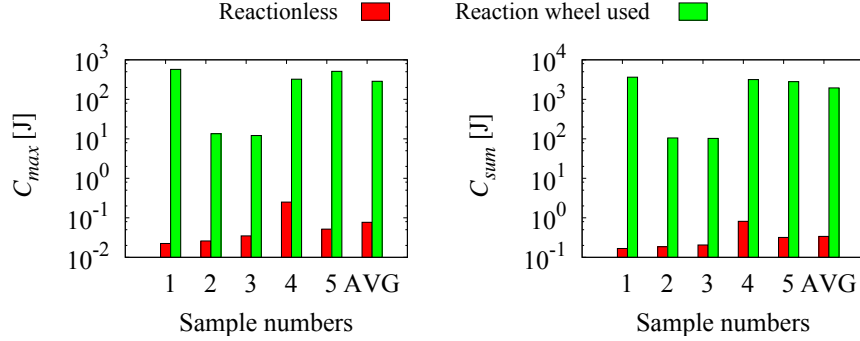


Fig. 5.5: Comparison of energy consumption under five conditions

reactionless motion control has an advantage in terms of energy consumption as described above. In addition, if we plan to perform this inspection task with reaction wheels, the manipulator has to be driven at lower speed because the limitation of the reaction wheel torque general poor: the limitation is 0.1 Nm in the ETS-VII.

Next we compare the cost over five conditions. The results are displayed with bar graph in Fig. 5.5. The red bar expresses the result under reactionless motion control; the green bar is that with the reaction wheels. Note that the axis of kinetic energy is represented as log scale. From the results, it can be seen that energy consumption under reactionless motion is also quite smaller than that of the reaction wheel based method. Actually, almost 10^3 times reduction is observed in the both cost functions. This result is due to the large energy consumption of reaction wheel as explained in (5.11). In summary, we can conclude that energy consumption can be largely reduced in addition to mission duration, by using reactionless motion control.

5.6 Summary

In this chapter, we discussed the energy consumption under zero attitude deviation. We formulated the kinetic energy of a free-floating space robot

in terms of joint velocity under zero attitude deviation. From the result, we confirm that the kinetic energy stemming from the reaction wheels is represented as a quadratic function of the inertia parameters of the manipulator and position vector positioning to the each line CoM, while the kinetic energy of the manipulator is a linear function of the both quantities. Hence, the energy consumption of the reaction wheels must be much larger than that of the manipulator. This feature makes reactionless motion control effectiveness in terms of energy consumption. In fact, from numerical verification, we showed that reactionless motion coincides with the instantaneous minimum energy motion. We compared the energy consumption of reactionless motion control with that of using reaction wheels during some inspection tasks that was proposed in Chapter 4. We obtain an interesting result that the kinetic energy during reactionless motions task is 10^3 times smaller than that during reaction wheel used task, on average. In summary, we can conclude that reactionless motion control has a advantage with respect to energy consumption.

Chapter 6

Formulation and Modeling

In this chapter, we describe motion/force control of redundant manipulators. First, we explain the Operational Space (OS) formulation that has been traditionally used under motion/force control and also impedance control by various researchers. Then, we describe a new control scheme based on Reaction Null-Space for motion/force control. Finally, the performance is confirmed through numerical simulations.

6.1 Formulations

6.1.1 OS formulation based control

From a historical point of view, we, firstly, explain the OS formulation based motion/force control in what follows.

Equation of motion in end-effector coordinates

Let us consider a serial n -link fixed base redundant manipulator as shown in the right part of Fig. 6.1. The model has n -active joints and n -rigid body links. We assume that the system has redundant DoF(s), i.e. $n > 6$. According to the OS formulation [37], the dynamics of a redundant serial-link

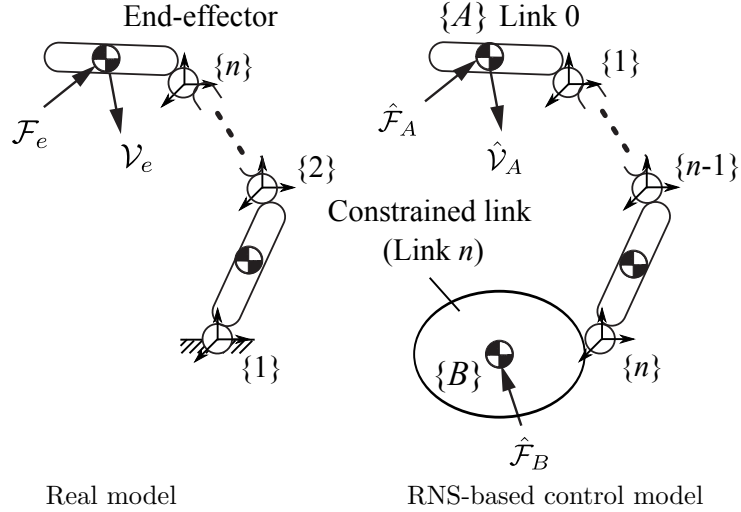


Fig. 6.1: Model of n -link manipulator model and its $n+1$ link control model for the RNS-based controller.

manipulator in end-effector coordinates are described in the following form:

$$\mathbf{M}_e \dot{\mathcal{V}}_e + \mathcal{C}_e + \mathcal{G}_g = \mathcal{F}_e + \mathcal{F}_\kappa \quad (6.1)$$

where $\mathcal{V}_e \in \mathbb{R}^6$ is spatial velocity of the end-effector, $\mathbf{M}_e \in \mathbb{R}^{6 \times 6}$ defines the operational space inertia matrix, $\mathcal{C}_e, \mathcal{G}_g \in \mathbb{R}^6$ stand for Coriolis and centrifugal force and gravity force, respectively. $\mathcal{F}_e, \mathcal{F}_\kappa$ is control command with dimensions of force, and the contact force imposed on the end-effector from environments.

On the other hand, because the end-effector variables cannot become generalized coordinates on redundant manipulators, the above equation of motion cannot be obtained directly. Hence, a transformation is needed from the equation of motion in joint-space.

The equation of motion in joint space is described as follows:

$$\mathbf{M}_l \ddot{\boldsymbol{\theta}} + \mathbf{c}_l + \mathbf{g}_l = \boldsymbol{\tau} + \mathbf{J}_e^T \mathcal{F}_\kappa \quad (6.2)$$

where $\boldsymbol{\theta} \in \mathbb{R}^n$ stands for joint coordinate vector, $\mathbf{M}_l \in \mathbb{R}^{n \times n}$ is the joint-space

inertia matrix, \mathbf{c}_l , \mathbf{g}_l denote Coriolis and centrifugal force and gravity force vectors in joint-space, respectively. $\boldsymbol{\tau} \in \mathbb{R}^n$ is joint torque vector, $\mathbf{J}_e \in \mathbb{R}^{6 \times n}$ is the Jacobian associated with the end-effector

Through the Jacobian, the end-effector velocity/acceleration are related to the joint variables as follows:

$$\mathbf{v}_e = \mathbf{J}_e \dot{\boldsymbol{\theta}} \quad (6.3)$$

$$\dot{\mathbf{v}}_e = \mathbf{J}_e \ddot{\boldsymbol{\theta}} + \dot{\mathbf{J}}_e \dot{\boldsymbol{\theta}} \quad (6.4)$$

On the other hand, from the result of statics, end-effector force can be related to joint torque through the following equation:

$$\boldsymbol{\tau} = \mathbf{J}_e^T \mathcal{F}_e \quad (6.5)$$

From (6.2) to (6.5), we can obtain the following definitions of OS dynamics matrices/vectors:

$$\mathbf{M}_e = (\mathbf{J}_e \mathbf{M}_l^{-1} \mathbf{J}_e^T)^{-1} \quad (6.6)$$

$$\mathcal{C}_e = [\mathbf{J}_e^{M+}]^T \mathbf{c}_l - \mathbf{M}_e \dot{\mathbf{J}}_e \dot{\boldsymbol{\theta}} \quad (6.7)$$

$$\mathcal{G}_e = [\mathbf{J}_e^{M+}]^T \mathbf{g}_l \quad (6.8)$$

where $\mathbf{J}_e^{M+} = \mathbf{M}_l^{-1} \mathbf{J}_e^T \mathbf{M}_e$ is the inertia weighted generalized inverse of the Jacobian.

Control command

Consider now a motion/force control scenario wherein the end effector is partially constrained by the environment. The end-effector dynamics become

$$\mathcal{F}_e - \mathbf{M}_e \dot{\mathbf{v}}_e - \mathcal{C}_e - \mathcal{G}_e = \mathcal{F}_\kappa \quad (6.9)$$

To meet the control objective, a reference end-effector force is designed as

$$\mathcal{F}_e^{ref} = \mathcal{F}_m^{ref} + \mathcal{F}_\kappa^{ref} \quad (6.10)$$

$$\mathcal{F}_m^{ref} = \mathbf{M}_e \mathbf{S} \dot{\mathbf{v}}_e^{ref} + \mathcal{C}_e + \mathcal{G}_e \quad (6.11)$$

$$\mathcal{F}_\kappa^{ref} = \mathbf{S}_\perp \mathcal{F}_c^{ref} \quad (6.12)$$

where \mathcal{F}_m^{ref} and \mathcal{F}_κ^{ref} are two components referring to end-effector motion and contact force, respectively. $\mathbf{S} \in \mathbb{R}^{6 \times 6}$ is a selection matrix suitably defined to specify the unconstrained motion direction, while $\mathbf{S}_\perp \in \mathbb{R}^{6 \times 6}$ is its complement. $\dot{\mathcal{V}}_e^{ref}$ and \mathcal{F}_c^{ref} are reference value for the motion and force tasks, respectively, that usually involve feedback control terms.

Further on, since the manipulator is redundant, there is an infinite set of control joint torques that could be applied without affecting the resultant forces at the end-effector [37].

$$\boldsymbol{\tau} = \mathbf{J}_e^T \mathcal{F}_e^{ref} + (\mathbf{E} - \mathbf{J}_e^T \mathbf{J}_e^{M+}) \boldsymbol{\tau}_a \quad (6.13)$$

where $(\mathbf{E} - \mathbf{J}_e^T \mathbf{J}_e^{M+})$ denotes a projector onto the null-space of the transposed inertia-weighted generalized inverse of the Jacobian, \mathbf{E} standing for the $n \times n$ identity matrix. $\boldsymbol{\tau}_a$, an arbitrary joint torque vector, parametrizes (in a non-minimal way) the set of joint torques that do not impose any end-effector force. Moreover, there is also another infinite set of control joint torques that produce the same end-effector acceleration as a given end-effector force:

$$\boldsymbol{\tau} = \mathbf{M}_l \mathbf{J}^\# \mathbf{M}_e^{-1} \mathcal{F}_e^{ref} + \mathbf{M}_l (\mathbf{E} - \mathbf{J}_e^\# \mathbf{J}_e) \ddot{\boldsymbol{\theta}}_a \quad (6.14)$$

where $\ddot{\boldsymbol{\theta}}_a \in \mathbb{R}^n$ stands for an arbitrary joint acceleration vector, $(\circ)^\#$ denotes generalized inverse of the corresponding matrix. The two joint-torque sets (6.13) and (6.14) are compatible (or dynamically consistent), only when the inertia-weighted generalized inverse of the Jacobian is applied in (6.14). This leads to *complete dynamic decoupling* between the particular components responsible for the motion/force control task and the null-space components.

The property of complete dynamic decoupling plays an important role in motion/force and impedance control design, since task and null-space control components can be designed independently. However, the nominal behavior in joint space determined by the task-space control component may become unstable due to ill-conditioning of the inertia weighted generalized inverse.

Also, the joint velocity may grow in an uncontrollable fashion because of the non-integrability of joint acceleration. Although these problems can be alleviated via the null-space control component, it would be much more desirable to have a controller with a satisfactory nominal behavior.

6.1.2 Reaction Null-Space based control

In what follows, we describe the RNS-based motion/force control for fixed-base redundant manipulators.

End-link dynamics based on free-floating base coordinates

For the RNS based motion/force control, we consider a free-floating base serial-link manipulator with $n+1$ links, as shown in the right part of Fig. 6.1. The two end-links are denoted as A and B . Without loss of generality, in what follows end-link A will be designed as the root link. It is convenient to assume that the root link is connected to the inertial frame via a virtual six-DoF joint. Hence, there are $n+6$ generalized coordinates: the n joint coordinated plus the six coordinates of the root end-link A . There are three points of interest: characteristic points on each of the two end-links (points A and B in Fig. 6.1) and the total center of mass. External spatial forces $\hat{\mathcal{F}}_A$ and $\hat{\mathcal{F}}_B$ act at points A and B , respectively. The motion of the two end-links is characterized by spatial velocities $\hat{\mathcal{V}}_A$ and $\hat{\mathcal{V}}_B$. Note that we distinguish the quantities of RNS based control model from these of the real model by using the notation $(\hat{\circ})$.

The system dynamics are described by two coupled equations:

$$\hat{\mathbf{M}}_A \dot{\hat{\mathcal{V}}}_A + \hat{\mathbf{M}}_{Al} \ddot{\hat{\boldsymbol{\theta}}} + \hat{\mathbf{C}}_A + \hat{\mathbf{G}}_A = \hat{\mathcal{F}}_A + \hat{\mathbf{T}} \hat{\mathcal{F}}_B \quad (6.15)$$

$$\hat{\mathbf{M}}_{Al}^T \dot{\hat{\mathcal{V}}}_A + \hat{\mathbf{M}}_l \ddot{\hat{\boldsymbol{\theta}}} + \hat{\mathbf{c}}_l \hat{\mathbf{g}}_l = \hat{\boldsymbol{\tau}} + \hat{\mathbf{J}}_B^T \hat{\mathcal{F}}_B \quad (6.16)$$

First, note that in (6.15) there are two linear force components. $\hat{\mathbf{M}}_{Al} \ddot{\hat{\boldsymbol{\theta}}}$ reflects the inertial coupling between end-link A and the rest of the links. Component

$\hat{\mathbf{M}}_A \dot{\hat{\mathcal{V}}}_A$, on the other hand, represents the inertia force of the composite rigid body (CRB) obtained when the joints are momentarily locked. The CRB dynamics are characterized by the inertial properties of the entire system; they are represented in terms of end-link A coordinates.

Next, note that (6.16) would represent the dynamics of a “conventional” fixed-base manipulator, where link A is fixed. This manipulator is composed of all bodies except link A ; because end-link A is the root, quantities $\hat{\mathbf{M}}_l$, $\hat{\mathbf{c}}_l$, $\hat{\mathbf{g}}_l$ and $\hat{\mathbf{J}}_B$ are those of the fixed-base manipulator, link B being its end-effector. To adapt this floating-base notation to the fixed-base manipulator described above, we will keep end-link A as the root link, but designate it as the end-effector. End link B , on the other hand, will be fully constrained to become the fixed base. This implies the renumbering of joints and links in reverse order, as illustrated in Fig. 6.1.

Control command

Our goal is to design a controller with a task-space control component that can ensure the desirable nominal behavior in joint space, such that large joint-velocity peaks and velocity build-up can be avoided. The derivation is based on the hybrid motion/force control approach presented in [38]. End-effector A contacts the environment under a motion/force task scenario, being thereby constrained along $k < 6$ directions. This can be expressed via the equation $\hat{\mathbf{J}}_\kappa(\dot{\hat{\mathbf{q}}})\dot{\hat{\mathbf{q}}} = \mathbf{0}$, $\hat{\mathbf{J}}_\kappa(\dot{\hat{\mathbf{q}}}) \in \mathbb{R}^{k \times (6+\kappa)}$ denoting the constraint Jacobian containing partial derivatives related to the environment constraint $\kappa(\dot{\hat{\mathbf{q}}}) = \text{const}$. End-effector A ’s spatial force is then $\hat{\mathcal{F}}_A = \hat{\mathbf{J}}_{\kappa A}^T \hat{\boldsymbol{\lambda}}$, where $\hat{\boldsymbol{\lambda}} \in \mathbb{R}^k$ is the Lagrange multiplier for the forces of constraint and $\hat{\mathbf{J}}_{\kappa A}(\dot{\hat{\mathbf{q}}}) \in \mathbb{R}^{k \times 6}$ is a submatrix of the constraint Jacobian s.t. $\hat{\mathbf{J}}_{\kappa A} \hat{\mathcal{V}}_A = \mathbf{0}$. Further on, denote $\hat{\mathcal{V}}_A = \hat{\mathbf{S}}_v \hat{\boldsymbol{\nu}}_A$ where $\hat{\boldsymbol{\nu}}_A$ is end-effector A ’s velocity along the unconstrained directions and $\hat{\mathbf{S}}_v(\dot{\hat{\mathbf{q}}})$ is defined from $\hat{\mathbf{S}}_f^T \hat{\mathbf{S}}_v = \mathbf{0}$, $\hat{\mathbf{S}}_f = \hat{\mathbf{J}}_{\kappa A}^T(\dot{\hat{\mathbf{q}}})$.

Using (6.15), we first obtain the reference joint acceleration for the task-

space (particular-solution) control component:

$$\ddot{\boldsymbol{\theta}} = \hat{\mathbf{M}}_{Al}^+(\hat{\mathbf{S}}_f \hat{\mathbf{f}}_\lambda - \hat{\mathbf{M}}_A \hat{\mathbf{S}}_v \hat{\boldsymbol{\alpha}}_v - \hat{\mathbf{M}}_A \dot{\hat{\mathbf{S}}}_v \hat{\boldsymbol{\nu}}) + \hat{\mathbf{M}}_{Al}^+(\hat{\mathbf{T}} \hat{\mathcal{F}}_B - \hat{\mathcal{C}}_B - \hat{\mathcal{G}}_B) \quad (6.17)$$

This control acceleration ensures complete decoupling between the motion and force subtasks for the closed-loop system. The respective joint torque control component derived via (6.16) is

$$\begin{aligned} \hat{\boldsymbol{\tau}}^{ref} = & (\hat{\mathbf{M}}_{Al}^T - \hat{\mathbf{M}}_l \hat{\mathbf{M}}_{Al}^+ \hat{\mathbf{M}}_A) \hat{\mathbf{S}}_v \hat{\boldsymbol{\alpha}}_v + \hat{\mathbf{M}}_l \hat{\mathbf{M}}_{Al}^+ \hat{\mathbf{S}}_f \hat{\mathbf{f}}_\lambda \\ & + (\hat{\mathbf{M}}_l \hat{\mathbf{M}}_{Al}^+ \hat{\mathbf{T}} - \hat{\mathbf{J}}_B^T) \hat{\mathcal{F}}_B \\ & + \hat{\mathbf{c}}_l + \hat{\mathbf{g}}_l - \hat{\mathbf{M}}_l \hat{\mathbf{M}}_{Al}^+ (\hat{\mathcal{C}}_A + \hat{\mathcal{G}}_A + \hat{\mathbf{M}}_A \dot{\hat{\mathbf{S}}}_v \hat{\boldsymbol{\nu}}) \end{aligned} \quad (6.18)$$

This control torque compensates the joint-space non-linear and gravity forces and ensures a double-integrator type closed-loop behavior $\ddot{\boldsymbol{\theta}} = \ddot{\boldsymbol{\theta}}^{ref}$. When compared to the particular-solution control torque derived under the OS formulation, $\boldsymbol{\tau} = \mathbf{J}_e^T \mathcal{F}_e^{ref}$, \mathcal{F}_e^{ref} given in (6.10), the above expression is somewhat messier. But we can expect a better nominal behavior in joint-space, as explained. The following remarks are due. First, note that with the controller we have to compensate the exact non-linear force term $\hat{\mathcal{C}}_A$ instead of compensating its approximation $\hat{\mathcal{C}}_A \approx \dot{\hat{\mathbf{M}}}_A \hat{\mathcal{V}}_A + \hat{\mathbf{M}}_{Al} \dot{\boldsymbol{\theta}}$ that was required for momentum conservation; otherwise, the task-space behavior cannot be guaranteed anymore.

Constraint force

To implement the RNS-based control, a constraint force that makes the link B the fixed base has to be presented. The constraint force is obtained through method of Lagrange multiplier in what follows.

First, we obtain the kinematic equation of the constrained link velocity as follows:

$$\begin{aligned} \hat{\mathcal{V}}_B &= \hat{\mathbf{T}}^T \hat{\mathcal{V}}_A + \hat{\mathbf{J}}_B \dot{\boldsymbol{\theta}} \\ &= \hat{\mathbf{J}}_{const} \dot{\hat{\mathbf{q}}} \end{aligned} \quad (6.19)$$

where $\hat{\mathbf{J}}_{const} = [\hat{\mathbf{T}} \ \hat{\mathbf{J}}] \in \mathbb{R}^{6 \times (n+6)}$ stands for constraint Jacobian, $\dot{\mathbf{q}} = [\mathcal{V}_A^T \ \dot{\boldsymbol{\theta}}^T]^T$ denotes the generalized velocity vector. Since the condition of fixed base is $\mathcal{V}_B = \mathbf{0}$, the following equation, hence, has to be satisfied:

$$\hat{\mathbf{J}}_{const} \ddot{\mathbf{q}} + \dot{\hat{\mathbf{J}}}_{const} \dot{\mathbf{q}} = \mathbf{0} \quad (6.20)$$

On the other hand, we can rewrite the equation of motion of the control model as follows:

$$\hat{\mathbf{M}}\ddot{\mathbf{q}} + \hat{\mathbf{c}} + \hat{\mathbf{g}} = \hat{\mathbf{Q}} + \hat{\mathbf{J}}_{const}^T \hat{\mathcal{F}}_B \quad (6.21)$$

Then, substituting (6.21) into (6.20) and solving it for $\hat{\mathcal{F}}_B$, we can obtain the constraint force as follows:

$$\hat{\mathcal{F}}_B = (\hat{\mathbf{J}}_{const} \hat{\mathbf{M}}^{-1} \hat{\mathbf{J}}_{const}^T)^{-1} \left(\hat{\mathbf{J}}_{const} \hat{\mathbf{M}}^{-1} (\hat{\mathbf{c}} + \hat{\mathbf{g}} - \hat{\mathbf{Q}}) - \dot{\hat{\mathbf{J}}}_{const} \dot{\mathbf{q}} \right) \quad (6.22)$$

Finally, the constraint force is substituting into (6.17) and (6.18).

6.2 Examples

6.2.1 Planar three-DoF manipulator

In what follows, we provide two examples for the motion/force controller. First, we consider a planar three-DoF redundant manipulator as shown in Fig. 6.2 (a). We assume that the end-effector contact with an environment at a point. Contact force acting to the end-effector has only force component; moment component is ignored. And also the end-effector orientation is not considered here. Hence, the system has one degree-of-redundancy.

Its control model is displayed in Fig. 6.2 (b). As shown in the figure, link 3 of the control model is regarded as the constrained link. The equation of motion of the control model is written as follows:

$$\begin{bmatrix} \hat{\mathbf{M}}_v & \hat{\mathbf{M}}_{v\omega} & \hat{\mathbf{M}}_{vl} \\ \hat{\mathbf{M}}_{v\omega}^T & \hat{\mathbf{M}}_\omega & \hat{\mathbf{M}}_{\omega l} \\ \hat{\mathbf{M}}_{vl}^T & \hat{\mathbf{M}}_{\omega l}^T & \hat{\mathbf{M}}_l \end{bmatrix} \begin{bmatrix} \hat{\mathbf{v}}_A \\ \hat{\omega}_A \\ \ddot{\boldsymbol{\theta}} \end{bmatrix} + \begin{bmatrix} \hat{\mathbf{c}}_{vA} \\ \hat{\mathbf{c}}_{\omega A} \\ \hat{\mathbf{c}}_l \end{bmatrix} + \begin{bmatrix} \hat{\mathbf{g}}_{vA} \\ \hat{\mathbf{g}}_{\omega A} \\ \hat{\mathbf{g}}_l \end{bmatrix} = \begin{bmatrix} \hat{\mathbf{f}}_A \\ 0 \\ \hat{\boldsymbol{\tau}} \end{bmatrix} + \begin{bmatrix} \hat{\mathbf{T}} \\ \hat{\mathbf{J}}_B \end{bmatrix} \begin{bmatrix} \hat{\mathbf{f}}_B \\ \hat{\mathbf{n}}_B \end{bmatrix} \quad (6.23)$$

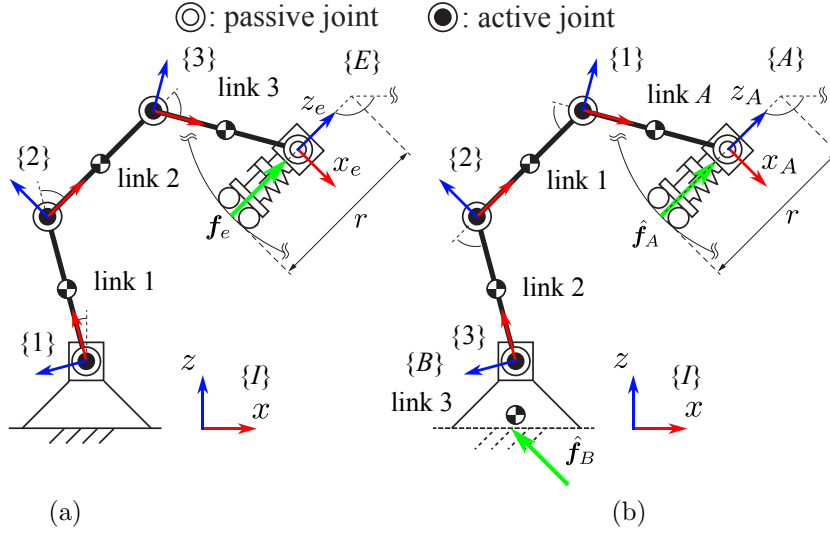


Fig. 6.2: Three-link planar redundant manipulator: (a) real model and (b) control model.

where the dimension of each coordinate are $\hat{\mathbf{v}}_A \in \mathbb{R}^2$, $\hat{\omega}_A$ and $\ddot{\boldsymbol{\theta}} \in \mathbb{R}^3$. Then, the size of the matrices is determined according to the dimension of the coordinate variables. Because we assume end-effector linear motion only, the equation of motion has to be modified. First, estimated from the middle part of (6.23), the angular acceleration of link A can be obtained as follows:

$$\dot{\omega}_A = -\hat{M}_\omega^{-1}(\hat{\mathbf{M}}_{v\omega}^T \dot{\mathbf{v}}_A + \hat{\mathbf{M}}_{\omega l} \ddot{\boldsymbol{\theta}} + \hat{c}_{\omega_A} + \hat{g}_{\omega_A} - \hat{\mathbf{T}}_\omega [\hat{\mathbf{f}}_B^T \quad \hat{n}_B]^T) \quad (6.24)$$

where $\hat{\mathbf{T}}_\omega \in \mathbb{R}^{1 \times 3}$ is the pose matrix associated with rotation. Then, substituting (6.24) into the upper part of (6.23), we can obtain the following equation of motion with reduced form:

$$\begin{aligned} & (\hat{\mathbf{M}}_v - \hat{\mathbf{M}}_{v\omega} \hat{M}_\omega^{-1} \hat{\mathbf{M}}_{v\omega}^T) \ddot{\mathbf{v}}_A + (\hat{\mathbf{M}}_{vl} - \hat{\mathbf{M}}_{v\omega} \hat{M}_\omega^{-1} \hat{\mathbf{M}}_{\omega l}) \ddot{\boldsymbol{\theta}} + \\ & (\hat{\mathbf{c}}_{v_A} - \hat{\mathbf{M}}_{v\omega} \hat{M}_\omega^{-1} \hat{c}_{\omega_A}) + (\hat{\mathbf{g}}_{v_A} - \hat{\mathbf{M}}_{v\omega} \hat{M}_\omega^{-1} \hat{g}_{\omega_A}) \\ & = (\hat{\mathbf{T}}_v - \hat{\mathbf{M}}_{v\omega} \hat{M}_\omega^{-1} \hat{\mathbf{T}}_\omega) [\hat{\mathbf{f}}_B^T \quad \hat{n}_B]^T \end{aligned} \quad (6.25)$$

Then, the reference joint acceleration can be obtained as:

$$\begin{aligned} \ddot{\boldsymbol{\theta}}^{ref} = & (\hat{\mathbf{M}}_{vl} - \hat{\mathbf{M}}_{v\omega} \hat{M}_{\omega}^{-1} \hat{\mathbf{M}}_{\omega l})^+ \left\{ (\hat{\mathbf{M}}_v - \hat{\mathbf{M}}_{v\omega} \hat{M}_{\omega}^{-1} \hat{\mathbf{M}}_{v\omega}^T) \ddot{\mathbf{v}}_A^{ref} + \right. \\ & (\hat{\mathbf{c}}_{v_A} - \hat{\mathbf{M}}_{v\omega} \hat{M}_{\omega} \hat{\mathbf{c}}_{\omega_A}) + (\hat{\mathbf{g}}_{v_A} - \hat{\mathbf{M}}_{v\omega} \hat{M}_{\omega} \hat{\mathbf{g}}_{\omega_A}) \\ & \left. - (\hat{\mathbf{T}}_v - \hat{\mathbf{M}}_{v\omega} \hat{M}_{\omega}^{-1} \hat{\mathbf{T}}_{\omega}) [\hat{\mathbf{f}}_B^{Tref} \quad \hat{n}_B]^T \right\} \end{aligned} \quad (6.26)$$

Parameters transformation

Under the RNS-based motion/force controller, we have to consider the relations of model parameters between the two models. End-effector coordinates, joint coordinate and joint torque are transformed according to the following role:

$$[\hat{x}_A \quad \hat{z}_A \quad \hat{\psi}_A]^T = [x_e \quad z_e \quad \psi_e]^T \quad (6.27)$$

$$[\hat{\theta}_1 \quad \hat{\theta}_2 \quad \hat{\theta}_3]^T = -[\theta_3 \quad \theta_2 \quad \theta_1]^T \quad (6.28)$$

$$[\hat{\tau}_1 \quad \hat{\tau}_2 \quad \hat{\tau}_3]^T = -[\tau_3 \quad \tau_2 \quad \tau_1]^T \quad (6.29)$$

In addition, the model parameters, such as link length, mass and inertia moment, are determined as follows:

$$[\hat{l}_A \quad \hat{l}_1 \quad \hat{l}_2 \quad \hat{l}_3]^T = [l_3 \quad l_2 \quad l_1 \quad l_3]^T \quad (6.30)$$

$$[\hat{m}_A \quad \hat{m}_1 \quad \hat{m}_2 \quad \hat{m}_3]^T = [m_3 \quad m_2 \quad m_1 \quad \hat{m}_3]^T \quad (6.31)$$

$$[\hat{I}_A \quad \hat{I}_1 \quad \hat{I}_2 \quad \hat{I}_3]^T = [I_3 \quad I_2 \quad I_1 \quad \hat{I}_3]^T \quad (6.32)$$

Note that the parameters of link 3 do not have a physical meaning because there is no corresponding part in the real model. Hence, these can be arbitrary values.

Simulation

We verify the performance of the RNS-based motion/force control with the three-DoF model. The initial configuration is set to $\boldsymbol{\theta} = [-105 \quad -50 \quad -$

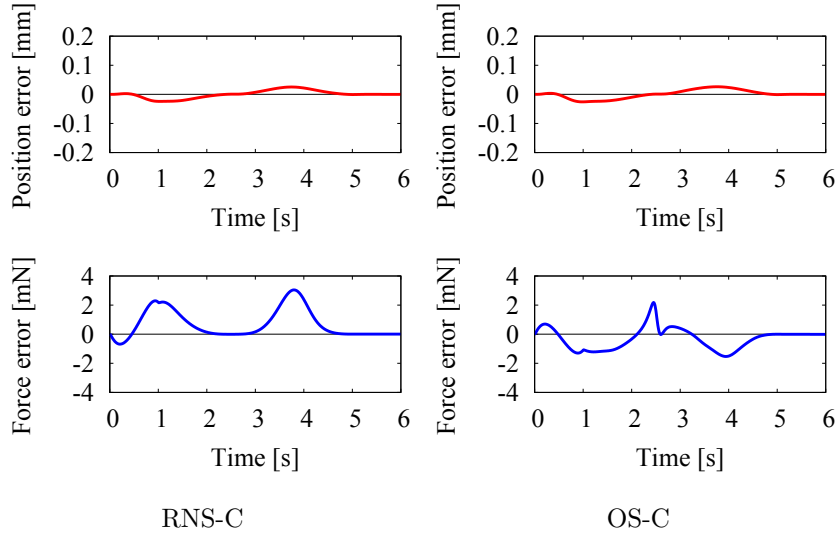


Fig. 6.3: Simulation results of end-effector position and force. The position error is along x -direction, while the force error is represented along z direction, in the end-effector frame.

60] T deg. The desired path in the unconstrained direction is defined via a fifth-order spline function, s.t. the end effector tracks the circular arc, whose center and radius are $[1.91 \ 1.91]^T$ m, of ± 45 deg in both directions (one full cycle). At the half cycle, the boundary conditions for the two splines are stationary, such that the end-effector pauses instantaneously. The feedback control loops for motion along unconstrained direction (x) is designed as

$$\hat{v}_{A_x}^{ref} = \hat{v}_{A_x}^{des} + k_d(\hat{v}_{A_x}^{des} - \hat{v}_{A_x}) + k_p(\hat{x}_{A_x}^{des} - \hat{x}_{A_x}) \quad (6.33)$$

where k_d and k_p are feedback gains. These are set at $k_d = 10 \text{ s}^{-1}$ and $k_p = 100 \text{ s}^{-2}$, respectively.

The desired force in the constrained direction z is designed as a fifth-order spline function during the first second, with a maximum value set at 10 N, to be kept constant for the remaining time. The feedback control loops for

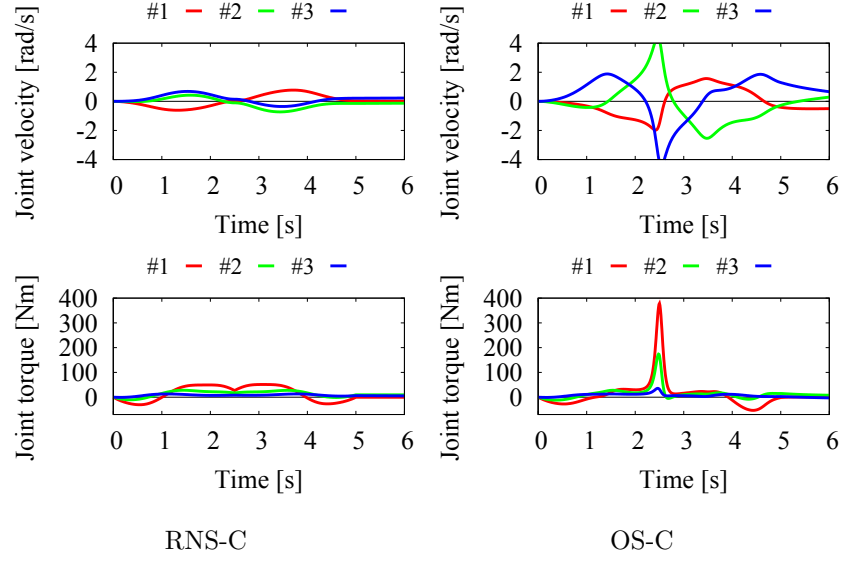


Fig. 6.4: Simulation results of the joint variables.

the force direction is designed as

$$\hat{f}_{Az}^{ref} = \hat{f}_{Az}^{des} + k_f(\hat{f}_{Az}^{des} - \hat{f}_{Az}) \quad (6.34)$$

where $k_f = 5$ is feedback gain. Note that the setting of the feedback gains is not critical due to the stability properties of the controller. The above values were selected empirically to yield minimal position/force tracking errors. In addition, we also executed the OS formulation under the same conditions for comparison. Note that, under the RNS-based control, the constrained link mass and length are set to $\hat{m}_3 = 10^5$ kg and $\hat{l}_3 = 0$ m. The role of the constrained link parameters will be mentioned in Chapter 7. Note that we assume zero gravity because gravity compensation induces a cyclic joint motion with a large velocity under the OS formulation based control. The reason will be mentioned in the next chapter.

Fig. 6.3 and Fig. 6.4 show the task and joint-space simulation results obtained with RNS-C and OS-C. From Fig. 6.3, it is apparent that the order of

end-effector position/force error are almost identical for the two controllers. This means that the properties of full motion/force decoupling could be validated with both controllers. Further on, from the joint-space behavior results shown in Fig. 6.4, it becomes apparent that the joint velocity obtained from the OS-C simulation undergoes much larger fluctuations than that in the RNS-C one; the respective peak values are 4.22 rad/s against 0.73 rad/s.

From these results, we can conclude that the RNS based motion/force control has a good capability as same as the OS formulation one does on the end-effector tracking performance. In addition, from the perspective of joint behavior, the RNS based control would be better performance than the OS formulation one.

6.2.2 Seven DoF redundant manipulator

Next, we verify the performance of the controllers with a seven-DoF redundant manipulator. The manipulator model is based on the arm of *Rollin' Justin*. The kinematic structure of the model and its control model for the RNS-based controller are depicted in Fig. 6.5. With this model, we straightforwardly use the control input describe in (6.18). The model parameters transformation would be done through the same manner in the case of the planar model. Namely, \hat{m}_7 , $\hat{\mathbf{I}}_7$ and \hat{l}_3 are the constrained link parameters of this model.

The initial configuration is set to $[20 \ -20 \ 0 \ 100 \ 0 \ 10 \ 0]^T$ deg. We assume that z direction in $\{E\}$ is the constrained direction due to the wall, while x - y plane in $\{E\}$ is the unconstrained direction as shown in Fig. 6.6. The desired motion path in the unconstrained direction is defined as a straight line along x -axis to $[0.24 \ 0.43 \ 0.43]^T$ m via fifth-order spline function. The desired motion is designed as a repeat motion between the initial position and the final one during 2.5 s, respectively. The desired force trajectory acting to z axis is defined as a fifth-order spline function during the first

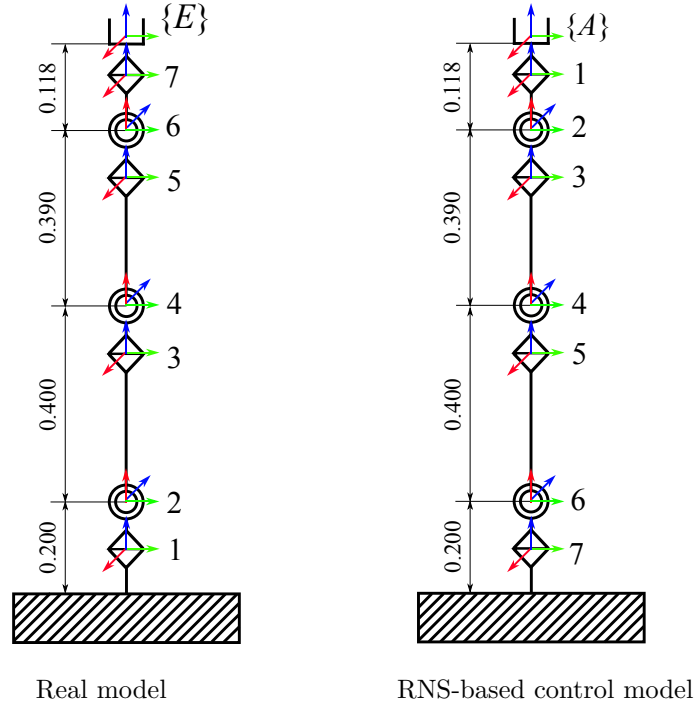


Fig. 6.5: Simulation model based on the arm of Rollin' Justin.

second, with a maximum value set at 10 N. In this case, simulation of the OS formulation is also executed under the same conditions. Note that, in both cases, orientation of the end-effector is fixed for the sake of simplicity.

Simulation results are displayed in Fig. 6.7 and Fig. 6.8. These quantities are measured in the inertial frame. From the results, it becomes apparent that the task-space behavior is almost identical for the two controllers. On the other hand, there is a different behavior in joint-space, especially joint velocity, in the same way as the planar case.

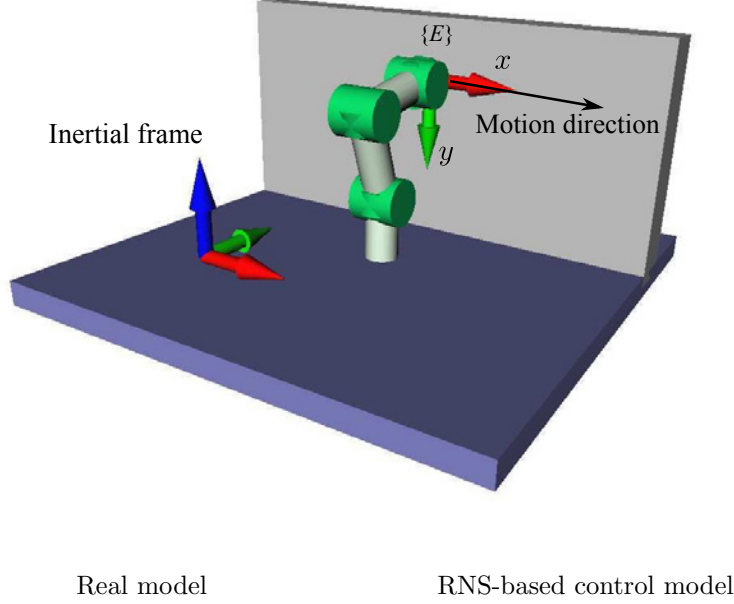


Fig. 6.6: Motion control direction is along x axis, while force control direction is along z axis, in the end-effector frame $\{E\}$.

6.3 Summary

This chapter described motion/force control methods. From a historical point of view, we first explained the OS formulation that has been used in various control schemes, such as hybrid motion/force control and impedance control. Then, a new introduced motion/force control method based on Reaction Null-Space was presented. Through numerical simulation with a planar and spatial models, we verified their performance from the perspective of both task-space and joint-space. It was confirmed that the task-space behaviors were almost identical for the two controllers. On the other hand, there is a difference between the two controllers in joint-space; the amplitude of joint velocities under the RNS-based control can be reduced smaller than

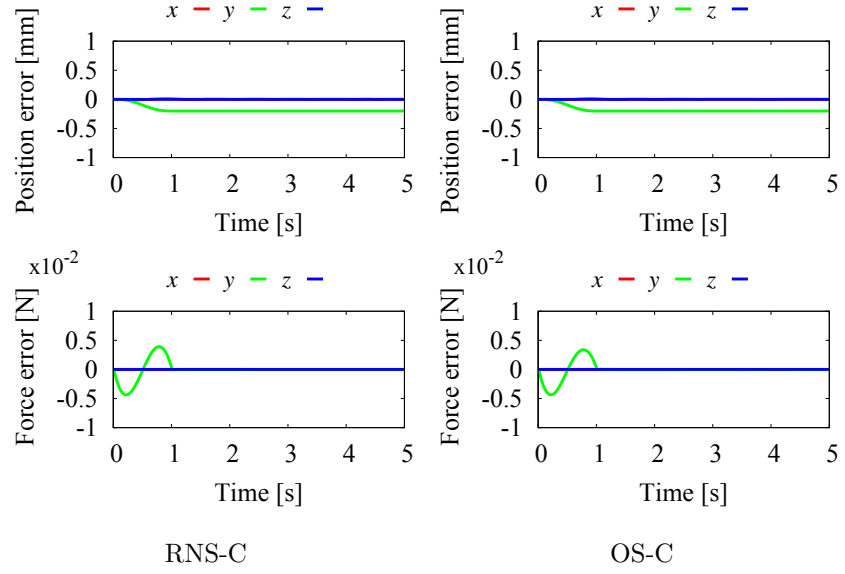


Fig. 6.7: Simulation results of end-effector position and force measured in the inertial frame.

that under the OS formulation.

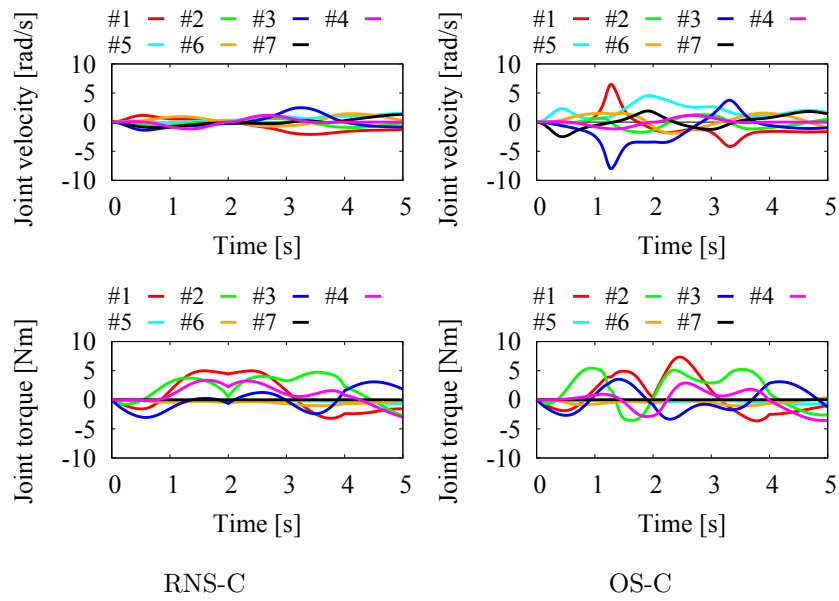


Fig. 6.8: Simulation results of joint-space behavior.

Chapter 7

Analysis on Joint Motion Behavior

In this chapter, we focus on the joint motion under the RNS-based motion/force control. As explained already in Chapter 6, the terminal link mass can be an arbitrary value at the control model. We examine the influence arising from change of the mass through numerical simulation.

7.1 Influence of the inertia parameter

As explained already in Chapter 6, the control model for the RNS-based control has an additional link compared to the real model. When we consider terrestrial manipulators, the meaning of the link is the ground. On the other hand, assuming unfixed base robots such as humanoids and space robots, the link is a floating base. In particular, in the case of fixed-base manipulators, the link parameters can be arbitrary values because these do not have a physical meaning. However, the parameters plays an important role under the RNS-based control, because the control method makes use of the dynamic coupling between the terminal link and other links. Hence, it is important to examine the influence of the inertia parameter. In what follows, we examine the influence with a planar model and the spatial model that is used in

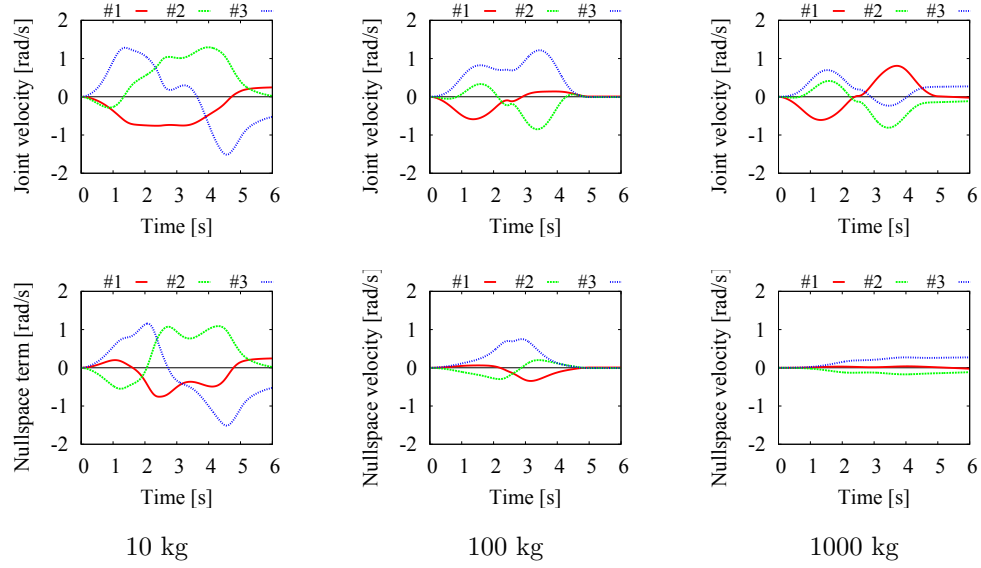


Fig. 7.1: The time profiles of the joint velocity and the null-space velocity: the upper part represents the joint velocity; the lower part is the null-space velocity, respectively.

Chapter 6, via numerical simulations.

7.1.1 Analysis through simulations

Let us consider a three-link planar model that is shown in Fig. 6.2. Fig. 6.2 (a) represents the real model, while Fig. 6.2 (b) is the control model. On the real model, we suppose that the each link mass is $m_i = 10$ kg, the each link length is $l_i = 1$ m, ($i = 1, 2, 3$). The constrained link mass is supposed to take the following values: 10, 100, 1000 kg. Of course, the inertia moment of the constrained link varies according to the mass. In addition, to focus on the joint motion, we assume that there is no interaction between the end-effector and an environment, without losing generality. The desired trajectory of the end-effector is a circular arc whose center is located on $[1.91, 1.91]^T$ m and radius is 0.707 m, respectively.

We show the time profile of the joint velocity and these null-space velocity in Fig. 7.1. In the figure, the upper part shows the joint velocity with the each constrained link mass; the lower part is the null-space velocity, respectively. From the results, we can confirm that the null-space velocity is gradually decreased, increasing the constrained link mass. Our concern is whether there is a motion to which the motion under the RNS-based control converge when the constrained link mass/inertia moment become massive. Actually, this motion exists and coincides with the minimum acceleration norm solution, which is obtained by resolved acceleration control with the particular solution only. In what follows, we discuss this interesting feature.

7.1.2 Discussion about the coincidence

Minimum acceleration constraint

First, we obtain the condition of the minimum acceleration norm solution. The equation describing the relation between end-effector acceleration and joint acceleration is written in the following form:

$$\dot{\mathcal{V}}_e = \mathbf{J}_e \ddot{\boldsymbol{\theta}} + \dot{\mathbf{J}}_e \dot{\boldsymbol{\theta}} \quad (7.1)$$

From the above equation, given an end-effector acceleration, the joint space can be divided into the two sub-space as follows:

$$\ddot{\boldsymbol{\theta}} = \mathbf{J}_e^+ (\dot{\mathcal{V}}_e - \dot{\mathbf{J}}_e \dot{\boldsymbol{\theta}}) + \mathbf{P}_J \ddot{\boldsymbol{\theta}}_a \quad (7.2)$$

where, $\mathbf{P}_J = \mathbf{E} - \mathbf{J}_e^+ \mathbf{J}_e \in \mathbb{R}^{n \times n}$ is the projection into the null-space of the Jacobian, $\ddot{\boldsymbol{\theta}}_a \in \mathbb{R}^n$ is an arbitrary vector with dimension of joint acceleration. The first term is the joint motion whose character is the minimum acceleration norm, the second term is the orthogonal term. We define the joint acceleration set \mathcal{Q}_J as (7.2). Using the motion decomposition of (7.2) is referred to as the resolved acceleration control.

The RNS constraint

Let us recall the constraint under the RNS-based control as follows:

$$\ddot{\boldsymbol{\theta}} = -\hat{\mathbf{M}}_{Al}^+(\hat{\mathbf{M}}_A\dot{\mathcal{V}}_A + \hat{\mathcal{C}}_A) + \hat{\mathbf{M}}_{Al}^+\hat{\mathbf{T}}\mathcal{F}_B + \hat{\mathbf{P}}_{RNS}\ddot{\boldsymbol{\theta}}_a \quad (7.3)$$

Note that we assume zero gravity environments without losing generality. Among these acceleration terms, we define a joint acceleration set related to the RNS-constraint as follows:

$$\mathcal{Q}_{M_{Al}} = \{\ddot{\boldsymbol{\theta}} \in \mathbb{R}^n | \ddot{\boldsymbol{\theta}} = -\hat{\mathbf{M}}_{Al}^+(\hat{\mathbf{M}}_A\dot{\mathcal{V}}_A + \hat{\mathcal{C}}_A) + \hat{\mathbf{P}}_{RNS}\ddot{\boldsymbol{\theta}}_a\} \quad (7.4)$$

This set consists of the accelerations appeared in (7.3) except the acceleration related to the constrained force. Namely, $\mathcal{Q}_{M_{Al}}$ represents the acceleration set that is satisfied with a completely free-floating model.

The interpretation

First, we assume that the order of the constrained link mass is same as the other links mass. In this case, $\mathcal{Q}_{M_{Al}}$ must differ from \mathcal{Q}_J , generally. Then, the constrained force related term acts to make the acceleration obtained from the RNS belong to \mathcal{Q}_J . The geometrical interpretation is shown in Fig. 7.2 (a). This is the mechanism that the RNS-based controller satisfies.

Next, we consider the case when the constrained link mass takes a huge value. In this case, linear and angular velocity of the constrained link become zero, according to the momenta conservation laws, as follows:

$$\hat{\mathbf{v}}_n = \lim_{\hat{m}_n \rightarrow \infty} \frac{1}{\hat{m}_n} \sum_{i=0}^{n-1} \hat{m}_i \hat{\mathbf{v}}_i = \mathbf{0} \quad (7.5)$$

$$\hat{\boldsymbol{\omega}}_n = \lim_{\hat{I}_n \rightarrow \infty} \sum_{i=0}^{n-1} \{\hat{I}_i \hat{\boldsymbol{\omega}}_i + \hat{m}_i \hat{\mathbf{r}}_i^\times \hat{\mathbf{v}}_i\} = \mathbf{0} \quad (7.6)$$

Therefore, the free-floating base robot behaves as a n -link fixed base robot even if there is no constrained force. This means that $\mathcal{Q}_{M_{Al}}$ gradually con-

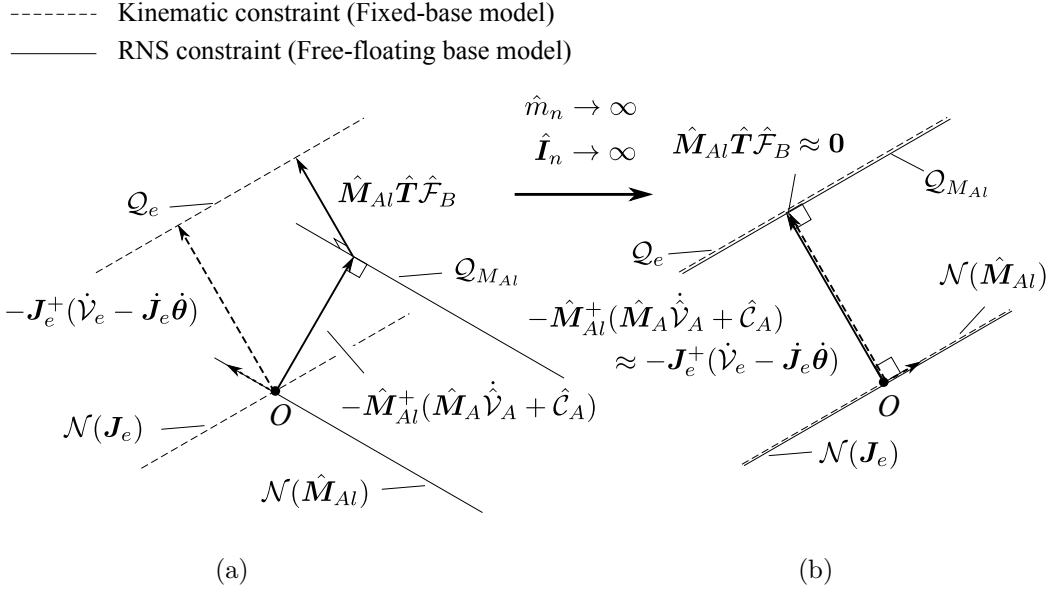


Fig. 7.2: A geometrical interpretation of the RNS constraint: (a) with a small mass of the constrained link and (b) with a large value of the mass.

verges to \mathcal{Q}_J , increasing the value of the constrained link mass. The interpretation is shown in Fig. 7.2 (b). Consequently, the motion under the RNS-based control coincides with that under the resolved acceleration control, i.e. minimum acceleration norm.

7.1.3 Verification via numerical simulations

In what follows, we verify the character through numerical simulations with the planar model. We compare a specific part of $\mathcal{Q}_{M_{Al}}$ with \mathcal{Q}_J under $\ddot{\boldsymbol{\theta}}_a = \mathbf{0}$ in the both set. The simulation conditions are the same ones used in Section 7.1.1. To evaluate the equivalence, we make use of the root mean square (RMS) of the motion error between under the RNS-based control and

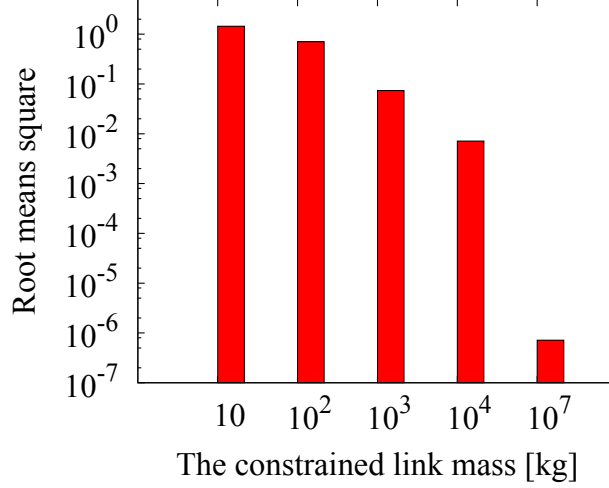


Fig. 7.3: The root means square of the motion error.

the resolved acceleration control as follows:

$$\text{RMS}[\Delta\theta] = \sqrt{\frac{1}{t_f - t_0} \int_{t_0}^{t_f} \|\Delta\theta(t)\|^2} \quad (7.7)$$

$$\Delta\theta(t) = \theta_{RNS}(t) - \theta_{RA}(t) \quad (7.8)$$

where θ_{RNS} and θ_{RA} stand for the joint motion under the RNS-based control and the resolved acceleration control, respectively.

The simulation results are displayed in Fig. 7.3. The simulations were conducted with some values of the constrained link mass. In the graph, note that y -axis is represented via log scale. From the results, we can confirm that the motion error described in (7.8) is gradually reduced, increasing the value of the constrained link mass. Hence, the character is proved.

7.2 Stabilization of joint motion

Despite acceleration based kinematic control schemes have advantages in terms of responsive and precis motion, there is a problem with instability of the joint motion. The problem have been discussed by several researchers [39–41]. In particular, it has been pointed out that the local torque optimization frequently falls into unstable. For this problem, an important analysis that clarifies the mechanism of the instability was done in [42]. In that work, the null-space acceleration/torque vectors that obtain the local torque minimization works as a positive feedback input on the null-space velocity. As a result, the instability can be observed. To obtain a stable behavior of the joint motion, it is mentioned that global optimization is necessary for torque minimization [43]. In the same work, some redundancy resolution schemes were also compared with a three-link model. These schemes are minimum acceleration norm, local torque minimization and the weighted minimum acceleration norm with the inertia matrix. Among them, the local torque minimization and the inertia weighted minimum acceleration schemes fell into unstable. On the other hand, the minimum acceleration norm did not become unstable, frequently. However, the method also can be unstable under specific conditions. An analysis indicated that all redundancy resolution schemes with dimension of acceleration can become unstable [42]: i.e. there is a finite escape time in all schemes.

As a different matter related to the instability, it is well-known that the null-space velocities remain at the end of motion, with acceleration based control methods.

To overcome these problems, velocity based acceleration control methods have been focused on by some researchers [44–46]. The solution is obtained as the time differential of velocity based solutions. The solution does not cause the instability because of the property of the minimum velocity norm

constraint. In [46], local torque minimization was carried out based on the velocity based methods.

As seen in Chapter 6 and Section 7.1.1, the remained joint velocity at the end of motion was observed. Under the RNS-based motion control, the same problem can happen as same as the kinematic schemes can. For the problem, we obtain the velocity based acceleration solution for the RNS-based control, in what follows.

7.2.1 The velocity-level based acceleration solution

We begin to formulate the solution, considering a velocity level equation. In this case, the velocity level equation is the momenta equations. These equations can be written as follows:

$$\hat{\mathbf{M}}_A \dot{\mathcal{V}}_A + \hat{\mathbf{M}}_{Al} \dot{\boldsymbol{\theta}} = \mathbf{0} \quad (7.9)$$

where, we assume no interaction and zero gravity, for the sake of simplicity. Given the assumption, we do not lose generality. Then, the velocity level solution can be obtained as follows:

$$\dot{\boldsymbol{\theta}} = -\hat{\mathbf{M}}_{Al}^+ \hat{\mathbf{M}}_A \mathcal{V}_A + \hat{\mathbf{P}}_{RNS} \ddot{\boldsymbol{\theta}}_a \quad (7.10)$$

Taking derivative of (7.10) in terms of time, we can obtain the velocity based acceleration solution as follows:

$$\ddot{\boldsymbol{\theta}} = -\hat{\mathbf{M}}_{Al}^+ (\hat{\mathbf{M}}_A \dot{\mathcal{V}}_A + \hat{\mathcal{C}}_A) + \hat{\mathbf{P}}_{RNS} (\ddot{\boldsymbol{\theta}} - \dot{\mathbf{M}}_{Al}^T (\hat{\mathbf{M}}_{Al} \hat{\mathbf{M}}_{Al}^T)^{-1} \hat{\mathbf{M}}_A \mathcal{V}_A) \quad (7.11)$$

where, we made use of the relation: $\hat{\mathcal{C}}_A \approx \dot{\mathbf{M}}_A \mathcal{V}_A + \dot{\mathbf{M}}_{Al} \dot{\boldsymbol{\theta}}$. Comparing (7.11) with (7.3), we can see that there is an additional acceleration term in (7.11), as follows:

$$\ddot{\boldsymbol{\theta}} = -\hat{\mathbf{P}}_{RNS} \dot{\mathbf{M}}_{Al}^T (\hat{\mathbf{M}}_{Al} \hat{\mathbf{M}}_{Al}^T)^{-1} \hat{\mathbf{M}}_A \mathcal{V}_A \quad (7.12)$$

The acceleration term obtains the minimum velocity norm constraint.

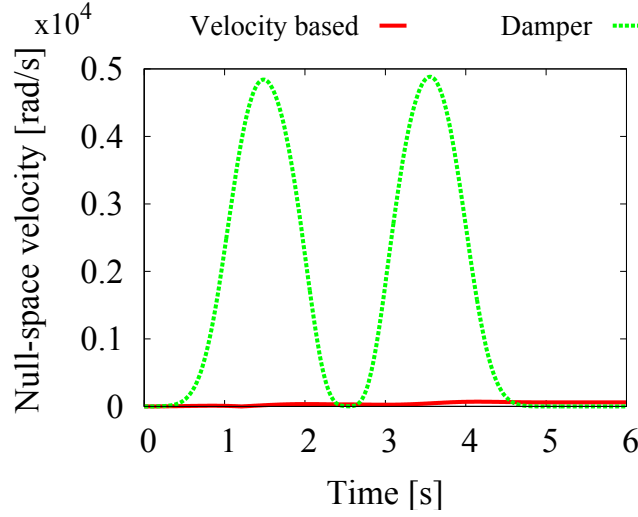


Fig. 7.4: Time profile of the Euclidean norm of the null-space velocity: the line in red represents the velocity based acceleration solution; the line in green stands for the velocity with the damper.

7.2.2 Verification via numerical simulations

Here, we verify the validness of the obtained solution through numerical simulations with the three-link planar model. The simulation conditions and the desired motion of the end-effector were the same ones that are used in Section 7.1.1. The constrained link was set to 10^4 kg.

To evaluate the validness, the resultant joint velocity is decomposed into the two parts as follows:

$$\dot{\boldsymbol{\theta}} = (\mathbf{E} - \hat{\mathbf{P}}_{RNS})\dot{\boldsymbol{\theta}} + \hat{\mathbf{P}}_{RNS}\dot{\boldsymbol{\theta}} \quad (7.13)$$

Under the minimum velocity norm condition, the second term in (7.13) must be zero. Hence, we make use of the Euclidean norm of the second term as the cost function. To obtain a comparative evaluation, we executed a simulation with adding a damping term into the null-space acceleration in (7.3): $\ddot{\boldsymbol{\theta}}_a = -\mathbf{K}_d\dot{\boldsymbol{\theta}}$. The value of the damper $\mathbf{K}_d = \text{diag}(k_d, k_d, k_d)$ was a high limit without causing instability: $k_d = 2770 \text{ s}^{-1}$.

We show the time profiles of the Euclidean norms in Fig. 7.4. In the graph, the line in red represents the velocity-level based solution; the line in green stands for the result with the damping term. Comparing with these results, we can see that the order of the null-space velocity with the damping is much larger than that with the velocity level-based solution. Hence, we can conclude that the proposed stabilization term has a good potential in terms of joint stabilization.

7.3 Summary

In this chapter, we discuss the joint motion under the RNS-based control. As an interesting character, we found out that the joint motion under the RNS-based control converges to that under the resolved acceleration control, increasing the constrained link mass.

As a different issue, we dealt with the instability of the joint motion arising from non-integrability of acceleration-level based control methods. We derived a velocity-level based acceleration solution to obtain a stable motion. This solution was verified via numerical simulation; that has a potential in terms of joint stabilization.

Chapter 8

Discussion and Future Research Directions

8.1 Conclusions

The aim of this work is developing control methods based on the Reaction Null-Space formulation for redundant manipulators. In particular, we tackled two control issues as: (i) reactionless motion control on free-floating space robots and (ii) motion/force control for redundant manipulators.

In the case of the first issue, we aimed to propose some tasks suitable for execution under reactionless motion control. First, we examined the properties of reactionless motion with a planar two-DoF model. Through vector field analysis, we confirmed that the manipulator attachment position plays an important role as a bifurcation parameter. Then, the reactionless motions of a seven-DoF redundant manipulator was discussed. From the perspective of the kinematic structure of the model, we represent reactionless motion of the model as superposition of the predominant wrist and elbow motion. Based on these motions, we proposed three motion tasks: (a) an inspection task using a hand camera, (b) a point-to-point positioning task and (c) a deployment task from a stowed configuration. The performances were verified through numerical simulation.

As an interesting feature of reactionless motion control, we found out that reactionless motion coincides with instantaneous minimum energy motion when no base-attitude deviation is assumed. This feature arises from the high energy consumption of reaction wheels. The kinetic energy to compensate the base reaction induced by manipulator motion is represented as a quadratic function of the manipulator parameters, while the kinetic energy of manipulator is a linear function. Hence, reactionless motion is feasible from the perspective of energy efficient due to no usage of reaction wheels. This feature was verified via numerical calculation. Finally, we compared the energy consumption of reactionless motion with that of reaction wheels used control system, under the inspection task explained above. From the above results, we can conclude that reactionless motion control is feasible from the perspective of both time and energy efficiency.

On the other hand, we proposed motion/force control based on the Reaction Null-Space formulation. We formulated the control scheme and verified it with a planar and a spatial model through numerical simulation. From the results, we confirmed that the performance of the task space control is as accurate as that of a method based on the Operational Space formulation, which is the most well-known/used method.

We found out that the joint motion under the Reaction Null-Space control coincides with that under the kinematic control with minimum acceleration norm solution, when the constrained link mass/inertia is massive.

As a different issue in redundancy, we tackled joint stabilization problem. It is known that unstable behavior of joint motion appears even when the task space is stable, due to the non-integrability of the control method. To this problem, we formulated a velocity-based stabilization term for the Reaction Null-Space control. Then, it was confirmed that the performance is better than that of a simple damping term.

8.2 Future tasks

We found out some feature of Reaction Null-Space controls. However, there are still important issues on both reactionless control and motion/force control. On reactionless motion control, we have to clarify the following things:

- Singularity of the coupling inertia matrix: Even the kinematic singularities have been much discussed, the singularity within the coupling inertia matrix has been unclear, so far. Because the matrix is highly nonlinear and complicated, we cannot discuss it analytically. So, we have to create numerical schemes that makes the singularities clarified.
- Manipulator design for reactionless motion control: In this work, we only dealt with a seven-DoF redundant manipulator. With the model, the position control of the end-effector under reactionless motion is impossible. However, position control of the end-effector can be used in several tasks such as assembly, inspection and construction and so on. Hence, we should improve the performance of the control method. One possible way is making use of appropriate manipulators for execution of reactionless motion control. By adding additional DoFs, we can expect that the movable region of the end-effector under reactionless motion runs.

On motion/force control, we have to consider as follows:

- Influences stemming from the particular solution component: We compared the proposed Reaction Null-Space based control with the Operational Space formulation based control. Then, it was confirmed that the control accuracy of task space was identical, while joint space behavior was quite different. Even so, if we add a null-space component, the two joint motions become a same one. Our concern is whether the particular components make the system dynamics different even when

a redundant control is executed. Especially we should discuss it from the perspective of zero dynamics.

Acknowledgment

Thanks

Submission date

Hiroki Sone

References

- [1] A. Flores-Abad, O. Ma, K. Pham, and S. Ulrich, “A review of space robotics technologies for on-orbit servicing,” *Progress in Aerospace Sciences*, vol. 68, pp. 1–26, Jul. 2014.
- [2] M. Oda, K. Kibe, and F. Yamagata, “ETS-VII, space robot in-orbit experiment satellite,” in *Proceedings of IEEE International Conference on Robotics and Automation*, vol. 1, 1997, pp. 739–744.
- [3] T. Yangsheng Xu, Kanade, *Space Robotics: Dynamics and Control*. Springer, 1993.
- [4] Y. Masutani, F. Miyazaki, and S. Arimoto, “Sensory feedback control for space manipulators,” in *Proceedings of IEEE International Conference on Robotics and Automation*, 1989, pp. 1346–1351.
- [5] K. Yoshida, “Engineering test satellite VII flight experiments for space robot dynamics and control: theories on laboratory test beds ten years ago, now in orbit,” *The International Journal of Robotics Research*, vol. 22, no. 5, pp. 321–335, 2003.

- [6] Y. Umetani and K. Yoshida, "Resolved motion rate control of space manipulators with generalized Jacobian matrix," *IEEE Transactions on Robotics and Automation*, vol. 5, no. 3, pp. 303–314, 1989.
- [7] S. Dubowsky and M. Torres, "Path planning for space manipulators to minimize spacecraft attitude disturbances," in *Proceedings of IEEE International Conference on Robotics and Automation*, 1991, pp. 2522–2528.
- [8] K. Yoshida, "Practical coordination control between satellite attitude and manipulator reaction dynamics based on computed momentum concept," in *Proceedings of IEEE/RSJ International Conference on Intelligent Robots and Systems (IROS'94)*, 1994, pp. 1578–1585.
- [9] F. Aghili, "Coordination control of a free-flying manipulator and its base attitude to capture and detumble a noncooperative satellite," in *Proceedings of IEEE/RSJ International Conference on Intelligent Robots and Systems*, Oct. 2009, pp. 2365–2372.
- [10] M. Torres and S. Dubowsky, "Path-planning for elastically constrained space manipulator systems," in *Proceedings of IEEE International Conference on Robotics and Automation*, 1993, pp. 812–817.
- [11] D. Nenchev, K. Yoshida, and Y. Umetani, "Analysis, design and control of free-flying space robots using fixed-attitude-restricted jacobian matrix," in *Proceedings of The Fifth International Symposium on Robotics Research*, 1990, pp. 251–258.
- [12] D. Nenchev, K. Yoshida, P. Vichitkulsawat, and M. Uchiyama, "Reaction null-space control of flexible structure mounted manipulator systems," *IEEE Transactions on Robotics and Automation*, vol. 15, no. 6, pp. 1011–1023, 1999.

- [13] D. Nenchev and K. Yoshida, “Impact analysis and post-impact motion control issues of a free-floating Space robot subject to a force impulse,” *IEEE Transactions on Robotics and Automation*, vol. 15, no. 3, pp. 548–557, Jun. 1999.
- [14] K. Yoshida, K. Hashizume, and S. Abiko, “Zero reaction maneuver: flight validation with ETS-VII space robot and extension to kinematically redundant arm,” in *Proceedings of IEEE International Conference on Robotics and Automation*, 2001, pp. 441–446.
- [15] D. Hirano, Y. Fujii, S. Abiko, R. Lampariello, K. Nagaoka, and K. Yoshida, “Simultaneous Control for End-Point Motion and Vibration Suppression of a Space Robot Based on Simple Dynamic Model,” in *Proceedings of IEEE International Conference on Robotics and Automation*, 2014, pp. 6631–6637.
- [16] T. Oki, H. Nakanishi, and K. Yoshida, “Whole-body motion control for capturing a tumbling target by a free-floating space robot,” in *Proceedings of IEEE/RSJ International Conference on Intelligent Robots and Systems*. IEEE, Oct. 2007, pp. 2256–2261.
- [17] N. Hara, D. Nenchev, and D. Sato, “Momentum conserving path tracking through dynamic singularities with a flexible-base redundant manipulator,” in *2010 IEEE/RSJ International Conference on Intelligent Robots and Systems*, 2010, pp. 5392–5397.
- [18] D. Dimitrov and K. Yoshida, “Utilization of the bias momentum approach for capturing a tumbling satellite,” in *Proceedings of IEEE/RSJ International Conference on Intelligent Robots and Systems*, 2004, pp. 3333–3338.

- [19] S. V. Shah, I. Sharf, and A. Misra, “Reactionless path planning strategies for capture of tumbling objects in space using a dual-arm robotic system,” in *Proceedings of AIAA Guidance, Navigation, and Control Conference*, Reston, Virginia, 2013.
- [20] K. Yoshida, D. Nenchev, P. Vichitkulsawat, H. Kobayashi, and M. Uchiyama, “Experiments on the PTP operations of a flexible structure mounted manipulator system,” *Proceedings of IEEE/RSJ International Conference on Intelligent Robots and Systems*, vol. 1, pp. 246–251, 1996.
- [21] A. Pisculli, L. Felicetti, P. Gasbarri, G. Palmerini, and M. Sabatini, “A reaction-null/Jacobian transpose control strategy with gravity gradient compensation for on-orbit space manipulators,” *Aerospace Science and Technology*, vol. 38, pp. 30–40, 2014.
- [22] H. Schaub and V. J. Lappas, “Redundant Reaction Wheel Torque Distribution Yielding Instantaneous L_2 Power-Optimal Spacecraft Attitude Control,” *Journal of Guidance, Control, and Dynamics*, vol. 32, no. 4, pp. 1269–1276, 2009.
- [23] M. D. Carpenter and M. A. Peck, “Dynamics of a High-Agility, Low-Power Imaging Payload,” *IEEE Transactions on Robotics*, vol. 24, no. 3, pp. 666–675, 2008.
- [24] M. Carpenter and M. Peck, “Reducing Base Reactions With Gyroscopic Actuation of Space-Robotic Systems,” *IEEE Transactions on Robotics*, vol. 25, no. 6, pp. 1262–1270, 2009.
- [25] Y. Nakamura and S. Ito, “Lowering energy consumption of Space robot systems through kinetic energy conservation,” in *Proceedings of IEEE International Conference on Robotics and Automation*, 1993, pp. 20–25.

- [26] R. Lampariello and G. Hirzinger, “Generating feasible trajectories for autonomous on-orbit grasping of spinning debris in a useful time,” in *Proceedings of IEEE/RSJ International Conference on Intelligent Robots and Systems*, 2013, pp. 5652–5659.
- [27] S. V. Shah and A. Gattupalli, “Energy Optimum Reactionless Path Planning for Capture of Tumbling Orbiting Objects using a Dual-Arm Robot,” in *Proceedings of the 1st International and 16th National Conference on Machines and Mechanisms*, 2013, pp. 16–21.
- [28] H. Sone and D. N. Nenchev, “On some practical reactionless motion tasks with a free-floating space robot,” in *Proceedings of IEEE International Conference on Robotics and Automation*, 2015, pp. 2836–2841.
- [29] Y. Nakamura, H. Hanafusa, and T. Yoshikawa, “Task-priority based redundancy control of robot manipulators,” *The International Journal of Robotics Research*, vol. 6, no. 2, pp. 3–15, 1987.
- [30] A. Dietrich, C. Ott, and A. Albu-Schaffer, “An overview of null space projections for redundant, torque-controlled robots,” *The International Journal of Robotics Research*, vol. 34, no. 11, pp. 1385–1400, sep 2015.
- [31] K. Kreutz-Delgado, M. Long, and H. Seraji, “Kinematic analysis of 7-DOF manipulators,” *The International Journal of Robotics Research*, vol. 11, no. 5, pp. 469–481, Oct. 1992.
- [32] R. Boudreau and R. Podhorodeski, “Singularity analysis of a kinematically simple class of 7-jointed revolute manipulators,” *Transactions of the Canadian Society for Mechanical Engineering*, vol. 34, no. 1, pp. 105–117, 2010.
- [33] S. Chiaverini, B. Siciliano, and O. Egeland, “Review of the damped least-squares inverse kinematics with experiments on an industrial

- robot manipulator,” *IEEE Transactions on Control Systems Technology*, vol. 2, no. 2, pp. 123–134, Jun. 1994.
- [34] D. N. Nenchev, “Singularity-Consistent Parameterization of Robot Motion and Control,” *The International Journal of Robotics Research*, vol. 19, no. 2, pp. 159–182, feb 2000.
- [35] S. Taki and D. Nenchev, “Euler angle based feedback control of large eigenaxis rotations in the presence of singularities and model uncertainty,” in *Proceedings of the 13th International Conference on Control, Automation and Systems*, 2013, pp. 34–39.
- [36] Y. Tsumaki, D. Nenchev, S. Kotera, and M. Uchiyama, “Teleoperation based on the adjoint Jacobian approach,” *IEEE Control Systems Magazine*, vol. 17, no. 1, pp. 53–62, 1997.
- [37] O. Khatib, “A unified approach for motion and force control of robot manipulators: The operational space formulation,” *IEEE Journal on Robotics and Automation*, vol. 3, no. 1, pp. 43–53, 1987.
- [38] L. Villani and J. De Schutter, “Force Control,” in *Springer Handbook of Robotics*. Springer Verlag, 2008, ch. 7, pp. 161–186.
- [39] K. O’Neil and Y.-C. Chen, “Instability of pseudoinverse acceleration control of redundant mechanisms,” in *Proceedings of IEEE International Conference on Robotics and Automation*, 2000, pp. 2575–2582.
- [40] K. A. O’Neil, “Divergence of linear acceleration-based redundancy resolution schemes,” *IEEE Transactions on Robotics and Automation*, vol. 18, no. 4, pp. 625–631, Aug. 2002.
- [41] J. Hollerbach and K. S. K. Suh, “Redundancy resolution of manipulators through torque optimization,” *Proceedings. 1985 IEEE International Conference on Robotics and Automation*, vol. 2, no. 4, 1985.

- [42] A. Maciejewski, “Kinetic limitations on the use of redundancy in robotic manipulators,” *IEEE Transactions on Robotics and Automation*, vol. 7, no. 2, pp. 205–210, 1991.
- [43] J. Hollerbach, “Local versus global torque optimization of redundant manipulators,” in *Proceedings of IEEE International Conference on Robotics and Automation*, 1987, pp. 619–624.
- [44] S. Ma and D. N. Nenchev, “Local torque minimization for redundant manipulators: a correct formulation,” *Robotica*, vol. 14, no. 2, pp. 235–239, 1996.
- [45] Y. Watanabe, “Acceleration-level analysis on velocity-based motion control of kinematically redundant manipulators,” in *Proceedings of IEEE/RSJ International Conference on Intelligent Robots and Systems.*, 2001, pp. 1–6.
- [46] Shugen Ma, “Local torque minimization of redundant manipulators with considering end-motion joint velocities,” in *1996 IEEE International Conference on Systems, Man and Cybernetics.*, 1996, pp. 1477–1482.